



U.S. DEPARTMENT OF  
**ENERGY**

PNNL-23831

Prepared for the U.S. Department of Energy  
under Contract DE-AC05-76RL01830

# Final Report: Property Improvement in CZT via Modeling and Processing Innovations – Te-particles in vertical gradient freeze CZT: Size and Spatial Distributions and Constitutional Supercooling

CH Henager, Jr. (PI)

KJ Alvine  
M Bliss  
BJ Riley  
JA Stave

October 2014



**Pacific Northwest**  
NATIONAL LABORATORY

*Proudly Operated by **Battelle** Since 1965*

## DISCLAIMER

This report was prepared as an account of work sponsored by an agency of the United States Government. Neither the United States Government nor any agency thereof, nor Battelle Memorial Institute, nor any of their employees, makes **any warranty, express or implied, or assumes any legal liability or responsibility for the accuracy, completeness, or usefulness of any information, apparatus, product, or process disclosed, or represents that its use would not infringe privately owned rights.** Reference herein to any specific commercial product, process, or service by trade name, trademark, manufacturer, or otherwise does not necessarily constitute or imply its endorsement, recommendation, or favoring by the United States Government or any agency thereof, or Battelle Memorial Institute. The views and opinions of authors expressed herein do not necessarily state or reflect those of the United States Government or any agency thereof.

PACIFIC NORTHWEST NATIONAL LABORATORY  
*operated by*  
BATTELLE  
*for the*  
UNITED STATES DEPARTMENT OF ENERGY  
*under Contract DE-AC05-76RL01830*

Printed in the United States of America

Available to DOE and DOE contractors from the  
Office of Scientific and Technical Information,  
P.O. Box 62, Oak Ridge, TN 37831-0062;  
ph: (865) 576-8401  
fax: (865) 576-5728  
email: [reports@adonis.osti.gov](mailto:reports@adonis.osti.gov)

Available to the public from the National Technical Information Service  
5301 Shawnee Rd., Alexandria, VA 22312  
ph: (800) 553-NTIS (6847)  
email: [orders@ntis.gov](mailto:orders@ntis.gov) <<http://www.ntis.gov/about/form.aspx>>  
Online ordering: <http://www.ntis.gov>



This document was printed on recycled paper.

(8/2010)

## **Te-particles in vertical gradient freeze CZT: Size and Spatial Distributions and Constitutional Supercooling**

CH Henager, Jr., KJ Alvine, M Bliss, BJ Riley, and JA Stave  
PNNL, Richland, WA 99352

### **Abstract**

A section of a vertical gradient freeze CZT boule approximately 2100-mm<sup>3</sup> with a planar area of 300-mm<sup>2</sup> was prepared and examined using transmitted IR microscopy at various magnifications to determine the three-dimensional spatial and size distributions of Te-particles over large longitudinal and radial length scales. The boule section was approximately 50-mm wide by 60-mm in length by 7-mm thick and was doubly polished for TIR work. Te-particles were imaged through the thickness using extended focal imaging to locate the particles in thickness planes spaced 15- $\mu$ m apart and then in plane of the image using xy-coordinates of the particle center of mass so that a true three dimensional particle map was assembled for a 1-mm by 45-mm longitudinal strip and for a 1-mm by 50-mm radial strip. Te-particle density distributions were determined as a function of longitudinal and radial positions in these strips, and treating the particles as vertices of a network created a 3D image of the particle spatial distribution. Te-particles exhibited a multi-modal log-normal size density distribution that indicated a slight preference for increasing size with longitudinal growth time, while showing a pronounced cellular network structure throughout the boule that can be correlated to dislocation network sizes in CZT. Higher magnification images revealed a typical Rayleigh-instability pearl string morphology with large and small satellite droplets. This study includes solidification experiments in small crucibles of 30:70 mixtures of Cd:Te to reduce the melting point below 1273 K (1000°C). These solidification experiments were performed over a wide range of cooling rates and clearly demonstrated a growth instability with Te-particle capture that is suggested to be responsible for one of the peaks in the size distribution using size discrimination visualization. The results are discussed with regard to a manifold Te-particle genesis history as 1) Te-particle direct capture from melt-solid growth instabilities, 2) Te-particle formation from dislocation core diffusion and the formation and breakup of Te-tubes, and 3) Te-particle formation due to classical nucleation and growth as precipitates.

## List of Figures

Figure 1. (a) TIR image of polished CZT section used for this study with the sections used for Te-particle analysis identified. (b) Optical image of the opposite half of the boule slice with a rough polish showing the individual grains. The shaded region in (a) is Section 1AF that is discussed later in the text.

Figure 2. Electron beam backscatter diffraction (EBSD) data for the growth tip region of the CZT boule studied here. The grain indicated by 2 in (a) and colored light green is the grain orientation imaged in sections 1 and 2, and most of 3 as shown in Fig. 1. The coloring is the key to the inverse pole figure plot shown in the inset in (a). A pole figure plot for this orientation is shown in (b) showing the near  $\langle 110 \rangle$  growth axis (circled pole).

Figure 3: (a) Composite optical micrographs from three different locations along section 1. Note that these micrographs combine all of the z-slices into one image such that all particles appear to be in focus at the same time. The smaller Te-particles are seen to be relatively evenly dispersed, while the larger particle distributions exhibit more variation. Facets can also be clearly observed on the larger Te-particles. Images (b) and (c) show higher magnification images with faceted large particles and strings of smaller particles. A twin boundary in (c) on the left side of the image is highly decorated with Te-particles.

Figure 4: Average Te-particle size distribution along section 1 of the boule, along the growth axis. The data (open circles) has been fit (red solid line) with a tri-modal log-normal distribution. Peaks in the distribution occur at 1.6  $\mu\text{m}$ , 7.3  $\mu\text{m}$ , and 11.8  $\mu\text{m}$ . Bimodal or higher complexity log-normal size distributions of Te-particles were observed to be typical in this sample.

Figure 5. The variation in Te-particle density along the growth direction (referenced to Fig. 1) for Section 1 of the large CZT boule over a distance of about 40-mm in length.

Figure 6. These plots show (a) the total, (b) less than 6  $\mu\text{m}$ , and (c) greater than 6  $\mu\text{m}$  diameter Te-particles radii over a distance of about 40-mm in length. These data are referenced back to Fig. 1: Section 1.

Figure 7. Schematic of Section 3 (radial section) with letter designations of regions of differing orientation denoted by the black arrows. The red and blue triangles denote the dominant orientation of the Te-particle tetrahedral, which will be detailed in the discussion.

Figure 8. Particle density statistics along the radial Section 3 is shown in the blue curve (See Fig. 1), while the red curve shows the longitudinal distribution from Fig. 4. The radial data also indicates a multimodal Te-particle distribution with a slightly higher density and larger particle peak size.

Figure 9. Log-normal plots of Te-particle distributions from the four separate grain regions shown in Fig. 7 in the radial direction together with representative TIR images from these regions.

Figure 10. Radial distribution function (pair correlation) for volume 1AF containing almost 32,000 Te-particles. Shown are the  $r_1$  and  $r_3$  pair correlations with the  $r_2$  distribution excluded from the data.  $r_1$  is strongly correlated at small distances, while  $r_3$  is correlated at larger distances only. Of most significance, the  $r_1$ - $r_3$  pairs are negatively correlated out to almost 250  $\mu\text{m}$ . A zone denuded of the smallest particles surrounds each large Te-particle.

Figure 11. Volume element 1G viewed in different methods to illustrate Te-particle distributions (see text for details). The image in (a) shows the flattened TIR image with the growth direction horizontal from left to right in the image. Image in (b) is the same volume element but now the Te-particles are color coded with respect to size. Magenta is largest ( $r_3$ ), teal is  $r_2$ , and bronze is  $r_1$ , the smallest size class. The  $r_1$  particles are removed to create image (c), which emphasizes the linear features of the  $r_2$  Te-particles. The volume element is rotated 90° about the growth axis to create image (d) to reveal that the  $r_2$  size Te-particles are clustered in a local region of the volume.

Figure 12. Intermediate size ( $r_2$  size class) Te-particles viewed from two perspectives from volume element 1G shown in Fig. 11. Image in (a) shows only the  $r_2$ -sized Te-particles that can be connected by bonds of length 200  $\mu\text{m}$  or less. The image in (b) is created by rotating the volume element so that the  $\langle 110 \rangle$ -direction is normal to the page and is oriented edge on to a (111)-type plane. Thus, the  $r_2$ -size Te-particles lie along  $\langle 110 \rangle$ -type direction on a (111)-type plane in this volume in the CZT boule.

Figure 13. Smallest Te-particles aligned along  $\langle 110 \rangle$ -directions and on (111) planes in volume element 2I. Image in (a) is flattened TIR image, (b) is an image of  $r_1$  Te-particles enlarged with  $r_2$  and  $r_3$  not visible. The  $\langle 110 \rangle$ -type directions are indicated with the dashed lines. Shown in (c) is the model rotated to bring (111)-type planes into edge on view.

Figure 14. Aligned Te-particles and rotated view showing planar alignment as well. (a) is an image of  $r_1$  Te-particles enlarged with  $r_2$  and  $r_3$  not visible. Shown in (b) is the model rotated to bring (111)-type planes into edge on view.

Figure 15. TIR image examples of quasi-periodic pearl-string formations within the boule. Shown in (a) are strings containing both  $r_1$  and  $r_2$ -sized Te-particles. Some of the strings have satellite  $r_1$  particles in between larger  $r_2$  particles. In the lower part of (a) solute trails are observed. These trails are not typical

of this CZT boule. Shown in (c) is a schematic of a Raleigh-Plateau thread break-up. The droplet wavelength observed here is consistent with this type of instability.

Figure 16. String-of-pearl image in volume element 2A near the growth heel with surrounding Te-particles removed to show the several collinear strings; one with clear satellite  $r_1$  Te-particles. The growth direction is left to right in (a). Shown in (b) is the same volume rotated to bring the (111)-type planes edge on in the view. Thus, all the strings lie along  $\langle 110 \rangle$ -type directions and on (1110)-type planes. Note the vertical spacing in (a) of several hundred microns.

Figure 17. Small crucible growth experiment at 11K/min cooling rate showing CdTe growth instabilities.

Figure 18. Optical image taken using a Nomarski prism of a small section of a growth from the  $\text{Cd}_{30}\text{Te}_{70}$  along with an EBSD map of small crucible growth at 1K/min cooling rate. Image in (a) shows  $\langle 110 \rangle$  growth instabilities near pinch-off with Te-particle faceting and solute trail formation. In (b) the EBSD map indicates large regions of single orientations and from this map the  $\langle 110 \rangle$  dendrite arms can be easily deduced.

Figure 19. Positions of  $r_1$  size class Te-particles from TIR microscopy in a volume element from section 1 after rotating the volume parallel to  $\langle 110 \rangle$  and edge on to (111)-type planes. Ribbons or planar arrangements of Te-particles are clearly visible in the spatial arrangement. The inset figure shows the 2D Fourier transform (averaged) of the spatial arrangement of the data. The 1D arrangement of peaks in the Fourier transform indicate a horizontal spacing of approximately 145 microns.

Figure 20. An image manipulated to show the large  $r_3$  Te-particles bonded to the nearest  $r_1$  Te-particles using stick bonds out to 250  $\mu\text{m}$ . The closest  $r_1$  to  $r_3$  distance in this volume element is 18  $\mu\text{m}$ .

## 1. Introduction

The need for high-purity cadmium-zinc-telluride (CZT) crystals for high-resolution radiation detection is well documented and many research groups are engaged in crystal growth of CZT [1-16], in fabrication of gamma-ray detectors from CZT [15, 17-23], and in the design of detector systems based on CZT [18, 24-38]. A ubiquitous problem for CZT crystals is the unwanted incorporation of Te-particles or Te-precipitates within the CZT crystal during the crystal growth process, in addition to other crystal defects. These defects have been shown repeatedly to affect the performance of CZT as a radiation detector material [10, 13, 39]. However, Te-particles are difficult to prevent during either Bridgman or traveling heater method (THM) growth due to the unfortunate characteristics of CZT at elevated temperature, namely, 1) poor thermal conductivity leading the high thermal strains during growth, 2) a small intrinsic stacking fault energy leading to easy twin formation, and 3) a low shear modulus coupled with a very small critical resolved shear stress for dislocation motion [40-42]. An excellent summary of these and other defects in CdTe is found in Ref. [40]. Specifically, Chapters VA and VB in Ref. [40] are valuable here as Refs. [41, 42].

The Rudolph group has hypotheses regarding the formation of Te-particles and precipitates in melt grown CZT and CdTe [41-47], which includes melt droplet capture at the melt-solid growth interface at preferred sites, such as re-entrant angles of grain boundaries and twins. Precipitates, on the other hand, form due to nonstoichiometric solid compositions typically due to the retrograde Te solubility in solid CdTe [41, 42]. Te-particles are typically on the order of a few microns in size or smaller, while Te-precipitates are 10 to 30-nm in size [41, 42, 44]. A common method of observing Te-particles is transmitted infrared (TIR) microscopy where inclusions down to about 1- $\mu\text{m}$  in diameter can be observed [44, 48, 49], while transmission electron microscopy (TEM) [50-52] or IR scattering techniques [48, 53]. In general, these observations and genesis hypotheses have been adopted by others [41, 42] and the convention adopted for this paper are that Te-particles are the same as Te-inclusions and are observable using TIR methods, but that Te-precipitates are much smaller and typically require TEM imaging.

Excess Te in the form of either precipitates or particles shows axial concentration profiles in vertical Bridgman, or equivalently, vertical gradient freeze (VGF) CZT growth [41, 48]. Te-precipitates are typically found to increase slightly in number density with respect to solidified fraction in Te excess melts with number densities on the order of  $10^{14}$  to  $10^{16} \text{ cm}^{-3}$  observed with sizes on the order of 10 to 20 nm [41, 48]. The Te-particles increase more significantly with axial location as a function of solidified fraction, which has been interpreted to suggest that this reflects a greater degree of Te melt enhancement as a function of solidified fraction in agreement with the growth of CZT using excess Te melts. While precipitation depends on the shape of the CdTe solidus, the amount of captured Te depends on the degree

of melt enrichment. Typical Te-particle concentrations range from  $10^5$  to  $10^8$   $\text{cm}^{-3}$  for sizes greater than about 1- $\mu\text{m}$ , which is about the observable limit of Te-particles using TIR.

Spatially, Te-particles are almost always associated with planar or extended defects in CdTe or CZT crystals, such as grain boundaries, twins, and dislocation subgrains [41, 42]. Te-particles form preferentially on grain boundaries and twins and the association with dislocations or subgrain boundaries is less clear. Morphologically, Te-particles are most often faceted particles embedded within the intersecting (111)-planes of CdTe or CZT as the host so that the Te-particles take on a tetrahedral shape with truncated corners [4, 41, 42]. The Te phase is most often the low-pressure trigonal or  $P3_121$  space group phase within the host lattice and can often be accompanied by large void space within the Te-particle reflecting the resolution of excess Te on cooling through the retrograde solubility region and the differences in thermal expansion between CdTe or CZT and Te [4, 41, 42]. Little lattice strain is observed in the host lattice due to the Te-particle, rather the Te region, which remains liquid below the freezing point of the host lattice displays severe mosaic patterns in electron backscatter diffraction (EBSD) indicating the misfit strains are accommodated completely within the Te-particles [4].

The purpose of this study is to refine observations of Te-particle distributions, both density and spatial distributions, in a well-characterized as-grown boule of CZT grown via the VGF method. This work combines high-resolution scanning TIR over large volumes with axial and radial extent that surpasses previous such studies. In addition, this study makes new observations with regard to Te-particle spatial distributions that make it possible to hypothesize in more detail the genesis of Te-particles in VGF grown CZT single crystals. These observations support many of the previous genesis theories as likely being accurate, but adds another method of particle genesis that appears to have been overlooked and is an important clue as to difficulties in growing CZT that is free of Te-particles. This study of Te-particles in VGF grown CZT is unique with regard to total observed CZT volume and with regard to the details of the TIR observations.

## **2. Experiment**

### ***2.1. Large CZT boule growth***

The CZT crystal examined in this study was grown using high-purity starting chemicals via the low-pressure Bridgman method, or VGF, with a nominal composition of  $(\text{Cd}_{0.9}\text{Zn}_{0.1})\text{Te}$  in a Mellen (The Mellen Company, Concord, NH, USA) Series EDG12-Sunfire 1200 C Programmable multi-zone furnace equipped with computer control over 18 separate heating zones, with 12 growth zones each 2.54-cm high and equipped with a mullite liner. Approximately 1-kg batch of CZT was melted in a lidded crucible (glassy carbon, Hochtemperatur-Werkstoffe GmbH, Thierhaupten, Germany) sealed within a GE224 quartz ampoule with an ingot diameter of 5.2-cm and a conical tip region with a  $43^\circ$  cone angle or  $94^\circ$

included angle tapered over a distance of 2.7-cm. The CZT charge was melted by following a thermal history/program consisting of 1) 28 hours at 1160°C to insure complete melting, 2) 8 hours at 1130°C, and 3) 264 hours of growth followed by 120 hours gradual cool-down cycle. The ampoule was first evacuated to  $\sim 10^{-4}$  Pa ( $10^{-6}$  Torr), flushed 3 times with a semiconductor-grade blend of hydrogen-argon (Matheson Argon ULSI 6N purity, with 2.6% H<sub>2</sub>) followed by evacuation, and sealed at  $\sim 3 \times 10^{-4}$  Pa ( $\sim 2 \times 10^{-6}$  Torr) with an oxy-propane torch, prior to melting. Once the vertical cooling gradient was established for the long growth run, the tip temperature was cycled between 1070°C and 1130°C to re-melt any nuclei formed at the tip in an attempt to select a single growth nucleus or dendrite. The growth rate was  $\sim 0.45$  mm/hour using 1.2°C/mm gradient [1].

### ***2.2. Small crucible solidification***

Approximately 12 g of pure CdTe plus pure Te to make a Cd<sub>30</sub>Te<sub>70</sub> ratio mixture from the same high-purity starting materials as for the large VGF growth were added to small glassy carbon cylindrical crucibles 13.3-cm diameter by 73-mm in height and melted at 1273 K for 24 h in a customized rocking furnace equipped with a water quench system. The Cd-Te mixture and crucible were vacuum-sealed in a quartz ampoule sized to fit inside a custom-made Inconel sleeve mounted inside the rocking furnace to prevent Cd or Te exposures due to ampoule breakage. The melts were cooled at varying rates including an air-quench rate, 11 K/m, 1.1 K/m and 0.1 K/m rates. The crucibles were removed, sectioned, and polished using colloidal silica to provide a cross-sectioned solid for further examination. These specimens were examined in a motorized stage microscope under polarized light using a Nomarski prism.

### ***2.3. TIR microscopy methods***

The TIR specimen was prepared by cutting a 5.3-mm thick slab of the entire CZT boule with a longitudinal cut using a slow speed wire saw so that the resulting sample, shown in Figure 1, was approximately 50-mm wide and 60-mm in length by 5.3-mm thick. It was doubly polished using diamond paste rough polishing and finished using colloidal silica. The sample was examined in an automated stage equipped microscope operated in the transmission mode using a Xenon lamp, IR filter, and a high-resolution IR camera.

The TIR data was used to generate a size distribution and 3D Cartesian coordinate data sets of Te-particles of sizes greater than about 0.5- $\mu$ m using an algorithm developed at PNNL. The algorithm post-processes the TIR z-sliced data to determine the through-thickness z-coordinate of the Te-particle via the embedded gray-scale parameter that is recorded for each particle determined as the z-sliced images are acquired. In this manner, each Te-particle is assigned an equivalent spherical size and a 3D-Cartesian coordinate with the z-coordinate constrained to individual through-thickness planes spaced 15- $\mu$ m apart.

### 3. Results

#### *3.1. Macroscopic TIR photos and EBSD data overlay*

The large CZT section analyzed here was previously studied [1] and the principal crystallographic growth directions of this unseeded growth were determined using EBSD methods. The growth direction of the large grains in the CZT section has been determined to be close to the  $\langle 110 \rangle$  and  $\langle 112 \rangle$  directions, which coincides with the fast growing directions observed in Ge dendrites by many others [54-60]. By analogy, we expect that CdTe and CZT will also exhibit fast growth along  $\langle 110 \rangle$  and  $\langle 112 \rangle$  due to similar crystallographic and kinetic attachment rates as for Ge [1]. The present study was performed using data from both single-oriented CZT grains, as well as from selected interfaces within the polished section (Fig. 1). The indicated crystallography in Figure 2 is from [1]. The pole figure plot of these two grains is shown in Fig. 2b and it is likely that these are the same grain wrapped around the cylindrical growth. The locations of the longitudinal and radial TIR traverses are shown in Fig. 1 and are labeled as sections 1, 2 or 3. Each of the single grains imaged in sections 1 and 2 are  $\sim \langle 110 \rangle$ -oriented along the growth direction, which is parallel to right-to-left in the image with the growth direction to the left, away from the tapered growth tip region. Each section was imaged in several volume elements consisting of regions either 2-mm or 3-mm or 4-mm long x 1-mm wide so that each sections 1 to 3 contain 12, 17, and 24 separate volume elements, respectively.

#### *3.2. TIR photos of regions of analysis*

Figure 3 shows composite optical micrographs from three different locations along Section 1 (see Fig. 1) with two higher magnification images also included, one showing a highly decorated twin boundary (Fig. 3c). Images such as these were acquired in Sections 1 to 3 from the large boule and analyzed for particle size and 3D Cartesian coordinate. These images are flattened Z-stack images where all the particles are in focus. The full set of images consists of several hundred Z-sliced images where the particles are only in focus within a single 15- $\mu\text{m}$  Z-slice. The algorithm picks out this Z-slice automatically from the embedded gray scale parameter tracked by the acquisition software. Each region of analysis typically contained several thousand Te-particles. The images were acquired to seamlessly cover the entire vertical or radial sections from Fig. 1 by stitching them together along the length of each section. However, each scanned region was also studied individually.

The images reveal a multimodal Te-particle distribution with some typical characteristics observed by others. First, the largest Te-particles are clearly faceted and previous work has shown that these particles are aligned with certain crystallographic planes in the CZT host lattice [4]. All of the large Te-particles in Fig. 3b are similarly oriented. Second, the facets lie along the traces of (111) planes in the CZT host lattice [4] and the rows of smaller particles also lie along (111) traces and are parallel to the large particle

facets. Third, extensive twin boundary decoration by Te-particles is observed in this material as shown in Fig. 3c.

### ***3.3. Particle size, density, and spatial distributions***

#### ***3.3.1. Size distribution data***

A particle density distribution and size analysis was performed on the Te-particles observed in the TIR microscope images taken across multiple locations on the boule. These measurements seek to establish the average and local Te-particle size distribution, as well as the evolution of the size distribution across the extent of the boule, including longitudinal and radial sections. This new information is valuable to aid in the understanding of the formation of the Te-particles and seeks to correlate distribution changes with growth positions. For these measurements as described above, the combination of available light transmission and time required per measurement indicated that a 200 times (20x objective) magnification was optimal. Based on the wavelength of light (NIR) and the NA of the objectives used, the minimum lateral resolution was approximately 0.5  $\mu\text{m}$  given by the diffraction limit, placing a lower bound on the Te-particle size distribution measured. Since the Te-particles are embedded somewhat randomly within the CZT matrix, other methods such as SEM and TEM [61] that might achieve higher resolution are significantly restricted. It is possible that X-ray or neutron tomography or small angle scattering might be employed to address this interesting issue, but that is beyond the scope of the current paper focusing on the distribution of micron scale Te-particles.

In addition to the lower lateral resolution limit imposed by diffraction, there is also a potential for undercounting, especially of smaller particles due to the finite number of “z-slices” taken. For each sample section, many focus depths, or “z-slices” are taken to image particles throughout the thickness of the sample. The typical spacing between focus depths in the vertical direction is 15 microns. This means that small particles lying between these focus points may be slightly out of focus- skewing the distribution to larger sizes or missing the smallest particles altogether. However, testing of 200 vs. 400 vs. 800 z-slices showed negligible difference in either number of particles or in the distribution. This is likely due to the fact that, at a minimum, the nearest neighbor particle distance is approximately 3 microns and that particles are still recorded even if slightly out of focus, and that the depth of field for that objective is likely on the same order. Slight changes in particle apparent size are within the uncertainty introduced by the binning of the data with radius to get reasonable statistics.

An averaged Te-particle size density distribution for boule section 1 (shown in Fig. 1) is shown in Figure 4. This data set represents the data averaged along the entire length of the section. The data (open circles) agrees reasonably well with a tri-modal log-normal distribution (red solid curve). This log-normal distribution is the norm for the Te-particle distribution probed locally within the boule. Also at each point

along the section, the distribution is typically bimodal, or trimodal, though higher orders were observed in certain locations. Log-normal size distributions are relatively common for a diversity of systems, including some complex nucleation and crystallization processes [62]. It should be noted that this log-normal distribution shown in Fig. 4 suggests the possibility of submicron particles which have been observed in the literature [61], but are beyond the scope of the current paper. The bulk of the particles observed are on average 1.6  $\mu\text{m}$  as indicated by the largest peak in the distribution. This small particle peak is typical of almost all locations of the sample indicating that these small particles are ubiquitous throughout the sample. The larger particle distribution peaks above 6  $\mu\text{m}$  vary across the sample and can exhibit one or more fairly sharp peaks depending on sampling location indicating that the large particle distribution varies throughout the sample (see Fig. 3). From the average distribution along section 1, the strongest peaks are at approximately 7  $\mu\text{m}$  and 12  $\mu\text{m}$ , which can be seen in these images.

While the resolution is not fine enough to discern facets on the smaller 1.6  $\mu\text{m}$  particles, facets can be easily observed on most of the larger Te-particles in Fig. 3. However, research on polished CZT specimens and SEM examinations [4] has shown that smaller Te-particles are likely faceted as well, since several of the Te-particles examined in [4] were only a few microns in size. The orientation of the facets on the larger particles appears to be nearly identical across section 1. This is to be expected since a comparison with Fig. 1 indicates that section 1 is contained nearly within a single crystalline grain. In addition, some pearl-line chains of particles are observed in the images. These chains can be made up of small or large particles with all of the particles nearly the same size within a chain, or alternating between two sizes. This may be indicative of a Raleigh-Plateau and will be discussed in more detail in a later section.

### ***3.3.2. Longitudinal (x)***

The data for Section 1 is shown as a function of longitudinal coordinate along the direction of growth as shown in Figures 5 and 6 and are referenced back to Fig. 1 with position along the boule starting at 0 for the growth heel, or end of growth, and 40-mm near the growth tip, or start of growth. The data covers about 40-mm in length (Fig. 1) and represents a unique set of data for Te-particles in melt grown CZT within a single grain orientation, which is determined to be almost parallel to the  $\langle 110 \rangle$  crystallographic direction along the growth axis. The density data shown in Fig. 5 indicates that the Te-particle density is almost constant over the growth extent and averages  $4.6 \times 10^5$  particles per  $\text{cm}^3$  as shown in Fig. 4. Fig. 6 shows how the Te-particle size classes vary over this growth extent. Here the total size distribution is flat and is dominated in number density by the smallest particles (see Fig. 4) but the largest particle size class, those greater than 6  $\mu\text{m}$  in diameter, decreases in average size in the growth direction over the 40-mm growth length in Section 1.

### 3.3.3. Radial (*r*)

Figure 7 shows the layout of the data acquired in the radial section, which is 50-mm in extent from edge-to-edge of the slab. The data acquisition region for the radial Te-particle distribution is very similar to that for the longitudinal data except that the radial section crosses several grain and twin boundaries whereas the longitudinal data was chosen within a single grain orientation. This likely accounts for the slight difference in Te-particle density in Section 3, the radial section, compared to the data shown in Section 1, the longitudinal one, which can be seen in Figure 8. The Te-particles are larger and have a higher number density on twin and grain boundaries, as shown in Fig. 3c. Including data from the twin and grain boundaries skews the average data towards larger particles and higher densities.

The radial data reveals additional interesting clues regarding Te-particle genesis and relationship to growth mechanisms if data from individual grain regions is compared. This data is grouped into separate grain-orientation regions as indicated in Fig. 7. In general, the data for all the grains is independent of their particular orientation is very similar but slight differences are noted here for later discussion. Region A-E consisted of 5 bins of TIR data within the same grain as the longitudinal data set that is grouped and plotted in Figure 9a as a log-normal density plot. The inset shows a typical TIR image from this region with an arrow indicating the growth direction drawn in Fig. 9a. Similar data is given for regions F-I (4 data bins within a separate grain), J-M (4 data bins within a separate grain), and N-X (11 data bins). These log-normal data along representative images are shown in Figs. 9b-d, respectively.

From previous work [4] it is known that faceted Te-particles are oriented within the CZT crystal aligned with (111) crystal planes of the CZT matrix phase. In the TIR images these faceted particles are 2D slices of the 3D tetrahedral-shaped particles (that are often truncated tetrahedrons), which appear as triangular shapes (cf. Fig. 3b) when viewed normal, or nearly normal, to a (111)-direction. Pole figure data for the grains imaged in Fig. 7 (see Fig. 2b) indicate that the large TIR slice is within 20° or 30° of the CZT- $\langle 111 \rangle$ . The triangles in Fig. 7 are drawn to correspond to the dominant triangular shapes in the various regions and the base of the triangle is parallel to the projected base of the faceted Te-particle tetrahedron. The base of the tetrahedron, and thus the edge of the triangle, is parallel to the  $\langle 110 \rangle$  crystal direction in CZT [4].

Te-particle data taken from region A-E is tri-modal with a peak at about 7  $\mu\text{m}$  and one at about 14  $\mu\text{m}$  and larger. Data from region F-I contains an inclined twin or grain boundary in the plane of the image, which affects the Te-particle size distribution data (Fig. 9b). The EBSD data orients the surface grain as nearly parallel to  $\langle 110 \rangle$  growth direction with about a 10° to 12° deviation from perfect  $\langle 110 \rangle$  so that this grain is similarly oriented compared to the larger grain in region A-E. The EBSD data indicates that the boundary between these two grains is a twin boundary. The majority of the particles seen in the inset image in Fig. 9b lie in a plane defined by the underlying twin or grain boundary that appears in the TIR

slab. The inclined boundary in the image is not indexed since it does not intersect the surface but the 3D dataset shows that this boundary is tilted at a  $5^\circ$  angle to the surface normal, which means that it is almost parallel to the growth direction. The Te-particle distribution shown in Fig. 9b is very similar for the small Te-particles compared to Fig. 9a but has a large peak at about  $10\ \mu\text{m}$  that appears to be associated with the 2D planar Te-particle distribution in the inclined boundary. The number density on this boundary is quite high and the  $10\text{-}\mu\text{m}$  size is quite uniform.

Region J-M also contains multiple inclined grains that do not intersect the surface but that contribute 2D planar Te-particle distributions and that affect the overall Te-particle distribution function (Fig. 9c). In this case the inclined plane is tilted at about  $40^\circ$  to the surface normal, but some of the data from this region is also from a continuation of the  $5^\circ$ -tilted planar defect from Region F-I. The EBSD data for this region indicates that the surface grain is oriented almost perfectly along a  $\langle 112 \rangle$ -direction so that the Te-particle tetrahedrons are oriented at  $30^\circ$  to the growth direction as required. The Te-particle distribution in this region includes peaks at about  $4$  to  $5\text{-}\mu\text{m}$ , a peak at about  $8\text{-}\mu\text{m}$  and another peak at a size just slightly larger than  $10\text{-}\mu\text{m}$ . The Te-particle density in the planar defects in this region is quite high and uniform in size compared to the 3D dataset.

Region N-X is oriented close to a  $\langle 110 \rangle$ -direction and Te-particle tetrahedra are aligned with the growth direction (Fig. 9d). No boundaries are included in this data set and the overall Te-particle distribution is a bi-modal distribution with smaller particles at slightly higher density compared to the longitudinal dataset and a larger Te-particle peak at about  $15\text{-}\mu\text{m}$  in size. This distribution lacks the peak at  $5$  to  $7\ \mu\text{m}$  that appears in many of the other size distributions.

### ***3.4. Pair Correlation and Spatial Data for Te-particles***

Although it is apparent from the TIR images from the CZT sections being studied that the Te-particles are not randomly distributed, it is important to analytically explore the spatial distribution in order to fully understand how these distributions may be connected to Te-particle genesis mechanisms. The use of pair-correlation tests and other methods can be helpful in this regard. Several representative volume elements have been chosen to explore the 3D spatial correlations. One large volume in Section 1 is considered and several smaller volumes in Sections 2 and 3 are also used for comparison. The large volume in Section 1 encompasses  $18\text{-mm}$  of longitudinal single crystal with nearly  $\langle 110 \rangle$  growth-axis orientation as discussed. This volume contains almost  $32,000$  Te-particles, with three different size distributions according to Fig. 8 (red curve) and three different bins were created to study the particles as:

$$\text{Bin 1: } 0 < r_1 < 6\ \mu\text{m}, \text{ Bin 2: } 6 \leq r_2 < 11, \text{ Bin 3: } 11 \leq r_3 \quad (1)$$

with the three radii chosen to match the tri-modal size distribution. The largest particles ( $r_3$ ) are faceted and the smallest particles ( $r_1$ ) are distributed log-normal as discussed. Both of these sizes are distributed

more or less randomly, but with some obvious spatial relation between these two size classes. The intermediate size particles ( $r_2$ ) are distributed in a different manner than either  $r_1$  or  $r_3$ . The spatial and orientation relations observed in this volume hold for all the volumes imaged in this study so that any examples shown here to aid this discussion are valid for all the volumes, and therefore, are assumed to be valid for this entire boule.

The volume in Section 1 labeled 1AF (see Fig. 1a) is 18-mm long in the growth direction ( $x$ ), 0.67-mm wide normal to the growth direction ( $y$ ) and 5.3-mm thick ( $z$ ), which provides a volume of  $63.9 \text{ mm}^3$  with an overall particle density of  $4.97 \times 10^5 \text{ cm}^{-3}$ . Out of the 31,768 particles in this volume 348 are in the largest size class,  $r_3$ , and 416 are in the intermediate size class,  $r_2$ . Figure 10 is the radial distribution function for volume 1AF for the  $r_1$  and  $r_3$  size classes, with the  $r_2$  class excluded since the  $r_2$  size class is distinctly differently organized. The  $r_1$  size class is strongly correlated at small distances from Fig. 10, while  $r_3$  is correlated at larger distances only. Of most significance, however, the  $r_1$ - $r_3$  pairs are negatively correlated out to almost 250  $\mu\text{m}$ . A zone denuded of the smallest particles surrounds each large Te-particle and this is readily observed in the 3D data sets.

Section 1G is shown in Figure 11 as an example of these three size distributions in a typical volume element. Fig. 11a is the flattened OM image showing the faceted Te-particles in the  $r_3$  size class, the strings of intermediate  $r_2$ -sized Te-particles, with the smaller  $r_1$ -sized Te-particles in the background, also showing some preferential alignment in particle strings. Fig. 11b shows the same image but now color-coded for the three size classes. The bronze particles are the  $r_1$  size class, the teal particles are the intermediate  $r_2$  size class, and the magenta particles are the largest  $r_3$  size class. It is apparent that the  $r_2$  Te-particles are aligned along specific directions and that some of the  $r_1$  Te-particles are similarly aligned. However, the  $r_3$  Te-particles are not obviously aligned in this image. Fig. 11c shows the same image as 11b but with the  $r_1$  size class removed to show the linear arrangement of the  $r_2$  Te-particles. Fig. 11d shows the same volume rotated by  $90^\circ$  about the  $x$ -axis (in the  $y$ - $z$  plane) to show that the  $r_2$  Te-particles are localized in the volume, and are not similarly related to the  $r_1$  or  $r_3$  Te-particle distributions

Referring to Fig. 11a, the faceted Te-particles are individually aligned with respect to the crystal axes such that the edge facets lie in (111)-planes of the CZT crystal and the edges are parallel to  $\langle 110 \rangle$ -type directions, similar to a Thompson tetrahedron [4]. Visually in Fig. 11a, it is obvious that the Te-particle strings lie along  $\langle 110 \rangle$ -type directions by virtue of being parallel to the visible edge facets. The angle with respect to the  $y$ -axis for these tetrahedral-edge directions, or  $\langle 110 \rangle$ -type directions, and Te-particle strings is about  $12^\circ$ , which is in agreement with the pole figure for this crystal (Fig. 2b) that shows that this crystal is oriented about  $12^\circ$  from the  $\langle 110 \rangle$ -type growth direction. When this volume is viewed from a perspective that places the orientation normal to  $\langle 110 \rangle$  then Figure 12a is generated, where only the  $r_2$

size class is visible. Viewed along a  $\langle 110 \rangle$ -direction in Fig. 12b, it becomes clear that the  $r_2$ -sized Te-particles are constrained to lie on a (111)-type plane in this volume. As mentioned above, however, this relation is almost universally true for all imaged volumes with few exceptions; including one where the  $r_2$ -sized Te-particles were observed on a (100)-type plane. Note also that the linear  $r_2$  features are separated by about 200  $\mu\text{m}$  or more in the plane of the growing CZT crystal (Figs. 11c and 12a).

Separately, volume 2I is shown in Figure 13 as an example of a volume containing very few  $r_2$ -sized Te-particles but one where the  $r_1$ -size class is quite obviously aligned along  $\langle 110 \rangle$ -directions and (111)-planes. Fig. 13a shows the flattened optical image with the large faceted  $r_3$  Te-particles clearly visible. Fig. 13b slightly enlarges the small  $r_1$  Te-particles and the  $r_2$  and  $r_3$  Te-particles are removed for clarity. Referring to Fig. 13a the traces of the  $\langle 110 \rangle$ -type directions are indicated on Fig. 13b and the alignments are obvious. When this particle model is rotated, however, it shows that many of these  $r_1$  Te-particles are not collinear. When viewed in projection along a  $\langle 110 \rangle$ -type direction (see Fig. 2) the view is nearly edge-on with respect to two (111)-type planes, and since the smallest Te-particles appear to have an affinity to collect on these planes then the projected view contains apparent lines of  $r_1$  Te-particles. It is clear that these linear features are aligned parallel with the edges of the faceted  $r_3$  Te-particles. When the 3D particle model is rotated by  $61^\circ$  about the x-axis and  $31^\circ$  about the y-axis to bring the view into a  $\langle 110 \rangle$ -type direction then two of the (111)-type planes appear edge-on with higher  $r_1$  Te-particle densities compared to a random distribution as shown in Fig. 13c.

When a similar volume element (2G) is rotated by  $78^\circ$  about the x-axis to bring the view nearly along a  $\langle 110 \rangle$ -type direction the location of two edge-on (111)-type planes becomes visible due to the alignment and collection of  $r_1$  Te-particles on these crystallographic features. The projected view in Figure 14a is shown with some of the aligned Te-particles highlighted and Fig. 14b shows the rotated view along  $\langle 110 \rangle$ . Both sets of images illustrate the crystallographic nature of the spatial distributions of the smallest Te-particles in certain regions.

### ***3.5. Pearl string morphology images***

Finally, one additional, but important, morphological features observed in various regions of the large boule are the so-called pearl-string features. Figure 15 shows a typical image of these features that can be observed in some of the imaged volume elements studied here. These occur more frequently near the boule tip and near the top of the boule at the end of the growth. Volume element 2A at the top of the boule at the end of the growth is shown in Figure 16 with several pearl-strings isolated by excluding the surrounding Te-particles. In this case, the strings all lie on a (111)-type plane that is inclined but parallel to the growth direction as shown in the rotated model in Fig. 16b. Similar to Fig. 13, these pearl-string features are also separated by roughly 200 microns and appear finger-like.

The images in Fig. 16 appear to be related to Rayleigh-type instabilities that develop in cylinders subject to surface diffusion and droplet formation due to surface tension. The formation of smaller satellite particles shown in Fig. 15a is typical of this type of instability. Fig. 16 shows that these instabilities are also confined to (111) planes in certain cases and are separated laterally by several hundred microns. Figs. 11 to 14 also show that these pearl-string features often lie along  $\langle 110 \rangle$ -type directions in the CZT crystal.

### ***3.6. Small Crucible Experiments***

The small crucible experiments demonstrated in a striking visual manner the growth instabilities observed and discussed in CdTe or CZT Bridgman growths. Figure 17 is an optical micrograph of a cross-section of one of the small crucible growths where the Cd:Te ratio was 30:70 to lower the melting point of the liquid to 1173 K (900°C). The cooling rate for this growth was 11K/min, which was suitable for demonstrating the growth front instability features. Fig. 18a shows a small single crystal CdTe region at the bottom of the crucible with a dendritic region above with long, straight  $\langle 110 \rangle$  dendrites as determined by EBSD. Fig. 18b is a high magnification image of one particular feature in the dendritic region of the growth showing a highly faceted dendrite with (111) edge facets and  $\langle 110 \rangle$ -oriented growth protrusions (or fingers). Entrained Te-particles in the dendrite are marked with arrows and regions about to “pinch-off” are marked. The growth fingers extend along  $\langle 110 \rangle$ -type directions and all facets in the images are (111)-type plane facets.

Figure 18 is an optical image in (a) and an EBSD map of a dendrite growth region showing that each dendrite is a region of single crystallinity in Fig. 18b. In each case, the dendrite arms lie along a  $\langle 110 \rangle$ -type direction in the CdTe lattice. Fig. 18a shows how individual fingers pinch-off and entrain large Te-particles or even Te-cylinders, or solute trails. Also note in Fig. 18a that the particles are faceted as they are entrained for slower growth rates (1K/min).

## **4. Discussion of Results**

### ***4.1. Constitutional supercooling and pattern formation***

The literature of crystal growth from the melt contains detailed descriptions of cellular growth and pattern formation, both with regard to dislocation networks and second-phase particles, due to constitutional supercooling [63-66], but only a few researchers document this for CZT growth [67-69]. This phenomenon is due to compositional changes at the solid-liquid interface leading to a supercooled liquid at the growth front, which can cause 1) morphological growth instabilities, 2) cellular growth, 3) solute trapping and/or solute trails, and 4) inhomogeneous solute distribution in the solid. It appears that the data presented in this paper can be sorted into several of these effects and, thus, much of the

interpretation offered here is from the perspective that the large, unseeded CZT boule studied here underwent constitutional supercooling during growth. Definitely, the small crucible growth experiments with the low-melting point liquid consisting of  $\text{Cd}_{30}\text{Te}_{70}$  starting ratio in the melt exhibited many examples of morphological instabilities due to this type of supercooling and compositional variations in the melt at the solid-liquid growth interface. Although the large CZT boule was not grown as fast as the small crucible growths and was grown from a melt that was nearly stoichiometric, nevertheless, the Te-particle patterning is suggestive of growth features observed in the small crucible experiments and from constitutional supercooling physics.

#### ***4.2. Spatial organization of particles and observable networks***

Previous work by our group has shown that the Te-particles are organized hierarchically [1, 4], i.e., local patterning reflected in higher-order patterning. Individual Te-particles are often observed to be faceted and it is understood from high-resolution EBSD data that the surrounding CZT is single crystal and the facets lie on the (111) planes of the underlying CdTe lattice, with the edges of the resulting tetrahedra lying along  $\langle 110 \rangle$ -type directions, while the Te-particle itself is a highly strained polycrystalline region [4]. Faceted Te-particles can be seen in many of the images presented here and constitute the largest size class of Te-particles, the  $r_3$  distribution having radii greater than or equal to 11- $\mu\text{m}$  in diameter. Particles like this can be seen forming during growth as entrained Te-particles in Figs. 17 and 18. There is a strong correlation between these largest Te-particles and the smallest size class as shown in Fig. 11. A spherical denuded zone surrounds each of the largest Te-particles with respect to the smallest size class,  $r_1$ , which suggests that the large  $r_3$  particles either did form due to solute entrainment or precipitated in special regions during the growth that possessed high diffusivity, such as dislocation cores. The most likely explanation, however, is the large particle entrainment process pictured in Figs. 17 and 18 such that these large Te-particles then served as efficient Te sinks to create the denuded zone. The  $r_3$  size class is apparently distributed randomly with respect to the growth direction or other crystallographic orientations that were studied here.

The smallest size class,  $r_1$ , is not randomly distributed and this is shown in Figs. 14 and 15. The size distribution is almost perfectly log-normal but the spatial distribution has three distinct features: 1) the denuded zone around the largest Te-particles is about 400- $\mu\text{m}$  in diameter and is quite spherical, 2) the planar or cellular patterning that aligns with crystallographic (111)-type planes, and 3) the  $\langle 110 \rangle$  linear features. The denuded zone connects the  $r_1$  and  $r_3$  size classes suggesting a common or interconnected genesis. The most likely explanation is that all the Te-particles form as a result of the morphological instabilities associated with constitutional supercooling and that the largest particles are entrained while the smaller ones precipitate out from solute-rich regions that develop around the growth instabilities, thus

creating the cellular structure from the supercooling. The intermediate  $r_2$  Te-particles are a special case of this type of formation and will be discussed further below. The patterning observed in the  $r_1$  size class follows the  $\langle 110 \rangle$ -type growth direction and the (111)-type planar alignment as has been observed in solutes in Ge growth studies [70, 71] and also by others in CZT growths [72-75]. Indeed, this cellular distribution is the hallmark signature of constitutional supercooling. In this case, although no attempts were made to image dislocations, a dislocation network may also be accompanying this cellular structure [72]. The formation of a dislocation network in CZT is a direct consequence of the low shear modulus at elevated temperatures during growth accompanied by growth stresses due to gravitational and crucible effects. The role of the supercooling and growth instabilities on dislocation creation during CZT growth is not known but it can be speculated that the pinch-off of growth instabilities along faceted (111) planes that are slightly misfitting may account for the creation of a dislocation network associated with the  $r_1$ -sized Te-particles. The  $\langle 110 \rangle$  linear features are thought to develop due to Rayleigh instabilities as discussed below.

The  $r_2$ -sized Te-particles are associated with very specific patterning in the CZT boule. Almost without exception this size class, which is not always present within the imaged volumes, is aligned along  $\langle 110 \rangle$ -type directions and on (111)-type planes but is more strongly associated with linear string-of-pearl features as shown in Fig. 15. The distinctions between the  $r_2$  size class and the  $r_1$  size class observed in these linear features are difficult to describe but they are not the same. The  $r_2$  Te-particles are often associated with strings having satellite Te-particles as in Fig. 15a. Further, these strings containing  $r_2$  Te-particles form collinear strings separated by several hundred microns and lie on (111)-type planes as shown in Figs. 12 and 16. These Te-particles are likely caused by solute trails that have broken up due to Rayleigh instabilities as shown in Fig. 15. The location of these Te-particles in certain regions of the CZT boule suggest that solute trail formation is the exception rather than the rule and signify regions of particularly severe growth instabilities compared to those regions absent of the  $r_2$  size class [74]. These  $r_2$  features are most often observed at the beginning and end of the boule growth, at the tip and then at the heel. The linear  $r_1$  features are aligned along  $\langle 110 \rangle$ -type directions but are more or less randomly located in certain growth regions. They are also likely to have formed collectively due to Rayleigh breakup.

#### ***4.3. Position dependence (x,r) vs. overall data***

This CZT boule, which was grown unseeded, develops a pronounced  $\langle 110 \rangle$  and  $\langle 112 \rangle$  growth axis at the periphery of the boule (see Figs. 1 and 2) with large grains that extend out to the edge of the boule that are likely the same grain that is wrapped around the central axis when viewed in this slab image. The boule center is a complex polycrystalline region with twins and grain boundaries. The growth tip is highly twinned with finer grains that eventually give way to the preferred  $\langle 110 \rangle$ - $\langle 112 \rangle$ -type growth directions

observed for this crystal structure [57, 60, 76]. Within the large single grains having  $\langle 110 \rangle$ -type growth direction, the number density of Te-particles and the size distributions are nominally constant with little variation from growth tip to growth heel. The Te-particle density increases slightly from tip to heel as shown in Fig. 5 but the fluctuation from region to region is quite large. Overall, the Te-particle densities measured here are in rough agreement with typical CZT data for VGF growth [72-75, 77, 78].

#### **4.3.1. Sizes**

The average Te-particle size is flat from tip to heel when all particles are considered. The average size of the  $r_1$  size class increases slightly from tip to heel, while the largest size classes,  $r_2$  and  $r_3$ , decrease in size more significantly from tip to heel. This behavior is consistent with coarsening during growth with those Te-particles at the growth tip having more time at temperature to grow at the expense of the smaller particles. The average size when considered as a function of radial position does not show significant trends and appears to be quite constant from edge to edge.

The size distributions, both radial and longitudinal and shown in Figs. 4 and 8, show a tri-modal distribution with peaks at 1.6, 7, and 12- $\mu\text{m}$  diameters for the longitudinal section. Section 3, the radial section, shows significantly higher overall densities and an intermediate size peak at 8.5- $\mu\text{m}$  compared to 7- $\mu\text{m}$  for the longitudinal sections. The largest peak is also shifted to slightly larger sizes and is less pronounced. The particle size distribution for this radial section is skewed relative to the longitudinal section by including several twin and grain boundaries, which tend to collect larger size particles compared to the single grain regions (see Figs. 9b and 9c that are from the radial section 3). Overall, there are significant differences from volume to volume within any one of the longitudinal or radial sections. Fig. 9d shows a bi-modal size distribution from a longitudinal section located almost midway between the growth tip and heel in section 1 (the actual image is from section 3 but where it intersects section 1). This region contains very few of the  $r_2$  size Te-particles as previously discussed. Fig. 9a, on the other hand, is also a volume from section 3 (where it intersects with section 2) and it clearly shows a tri-modal distribution and several string-of-pearl features containing many  $r_2$ -sized Te-particles. Thus, the size distribution functions are basically tri-modal with regions missing the  $r_2$  size peak where the growth was more stable.

#### **4.3.2. $g(r)$**

The corresponding pair correlation functions, or  $g(r)$  curves, for the large and small Te-particles ( $r_1$  and  $r_3$  sizes) shown in Fig. 10 quantifies some of the differences in these spatial distributions. The  $r_1$  pairs are strongly correlated small distances with no visible structure to the  $g(r)$  curve. Hints of small peaks at 40, 60, and 75- $\mu\text{m}$  distances reflect the weak cellular pattern spacing observed in many of the volume elements. One particular volume element was selected to explore this higher-level patterning using

Fourier transform methods and this is shown in Figure 19. A volume from section 1 was rotated to bring a  $\langle 110 \rangle$ -type direction parallel to the vertical axis of the image and the particle size was adjusted along with the black and white contrast to create Fig. 19. An averaged 2D Fourier transform image is shown in the upper right as an inset figure. The peaks in the inset are due to a horizontal spacing in the black and white image of about 145  $\mu\text{m}$ . Thus, the small peaks in the  $g(r)$  curve in Fig. 11 reflect this type of higher-level patterning. However, the  $g(r)$  curve mainly reflects the strong positive correlation between the small  $r_1$  Te-particles and the weak patterning at longer distances, in general. The ability of a pair correlation function to bring out this weak patterning is complemented by the Fourier transform data. The human eye can pick out longer-range patterns observed here much better than is possible with standard correlation functions.

The  $r_3$  pairs are not correlated at small distances but exhibit a peak in the 40 to 60  $\mu\text{m}$  range, another peak in the 130 to 170  $\mu\text{m}$  range, and a final peak at about 280  $\mu\text{m}$ . The significance of these peaks is not known. However, the  $r_1$ - $r_3$  correlation is revealed as a strong negative correlation (ignoring the small peak at 20  $\mu\text{m}$ ) out to a radial distance of about 200 to 250  $\mu\text{m}$ . Visually, it is observed, and this  $g(r)$  data supports, that each large  $r_3$ -sized Te-particle is surrounded by a nearly spherical region with a diameter of about 400 to 500  $\mu\text{m}$  denuded of the smaller  $r_1$  Te-particles. Figure 20 illustrates this with a 2D image of the spherical denuded zones illustrated with stick bonds between  $r_3$  and  $r_1$  particles. For this figure the bond length was chosen to be 250  $\mu\text{m}$  for illustrative purposes. The large Te-particles are strong sinks for the excess Te solute atoms during the crystal growth process. Since LSW coarsening theories do not predict the formation of bi-modal distributions from a starting log-normal distribution [79], it must be that the large Te-particles either form directly from the melt as suggested by Figs. 17 and 18 or that these large Te-particles lie on a fast diffusion path in the CZT lattice, such as on a dislocation core or dislocation node. The more likely explanation is that they are entrained directly from the melt and act as strong Te sinks during growth and cool-down to create the denuded region.

#### ***4.3.3. GBs and Twin Boundaries***

Volume elements in section 3 that contain twin or grain boundaries reveal that, as is well known for CZT crystals grown from the melt, these planar defects are strong sinks for Te-particles [72, 74, 75, 77]. The study of this or its implications are beyond the scope of this paper but without exception the boundaries imaged in this study always contained a large number of  $r_2$ -sized Te-particles and that these particles were constrained in the plane of the defect. Most likely this is due to the excess atomic volume associated with the planar defects and the Te-particles.

#### ***4.4. Linear formations of particles and Rayleigh instability***

As noted previously, pearl-string like formations where Te-particles of a similar size are arranged in a chain are observed to occur in many locations across the boule (see Figs. 12, 14, and 15). Strings may be comprised of either large or small diameter particles. In some cases (see Fig. 15a) satellite particles of a smaller size occur between the larger particles. These pearl-string like formations are typical of a Rayleigh-Plateau instability [80] that we hypothesize occurs during the cool down of the boule. The origins of the thread break-up Rayleigh-Plateau instability is shown schematically in Figure 15c. Te-rich threads or solute trails may occur in certain regions as a direct consequence of the constitutional supercooling. If a dislocation core is formed in the CZT matrix from growth instabilities preferential diffusion of Te along the dislocation could result in the formation of Te-rich threads within the solid CZT matrix. Or, the growth instabilities as they pinch-off as shown in Figs 17 and 18 can result in the formation of solute trails observed in many other systems. These threads in the surrounding CZT melt are unstable due to surface or interface tension and break up into droplets. This is facilitated by the preferential growth of specific wavelengths of thermal undulations in the thread surface. The resulting droplets then have a size and spacing related to the initial thread radius and the dominant mode as determined by volume conservation. In Figure 15a, there are also locations where dark lines appear between the Te-particles that are suggestive of Te-rich threads in support of the above arguments.

This Rayleigh-Plateau instability hypothesis may also partly explain the high density of particles along the traces of (111)-type planes as described in 4.2. In contrast, a perfect liquid sheet is stable to thermal surface perturbations [81, 82]. However, defects readily provide a pathway to sheet rupture with a similar result to the Rayleigh-Plateau instability, namely that of sheet rupture and droplet formation. It is this process that drives film dewetting [83]. This process would be envisioned to occur as Te-rich ribbons or planes are captured by the growth instabilities in a manner similar to how the large Te-particles are entrained (Figs. 17 and 18). However, a more simple precipitation process is also likely since the entrained regions between the growth instabilities would naturally have a higher Te concentration compared to the bulk crystal or bulk liquid.

It is also worth noting that the presence of smaller satellite particles in some of the pearl-string formations is suggestive of indicative of weak confinement during the break-up process [80], which is reasonable given that the interface between the Te and the CZT solid matrix would be broadened by diffusion. Given the depression of the melting point of the CZT with increasing Te, this would weaken the confinement of the threads by softening the surrounding matrix.

## 5. Conclusions

A large CZT boule was grown from the melt using VGF methods and examined using TIR microscopy to generate a large 3D dataset of Te-particles with concomitant size and spatial distribution data. The cylindrical CZT boule, which was tapered at the growth tip and was about 50-mm long and 50-mm in diameter, was sectioned longitudinally and polished for TIR microscopy as a slab with a thickness of about 7-mm. Several large grains having a growth axis nearly parallel to  $\langle 110 \rangle$  were imaged longitudinally and radially with two longitudinal sections and one radial section imaged from tip to heel.

In general, but not exclusively, a tri-modal size distribution of Te-particles was observed with an overall number density of about  $4.6 \times 10^5$  Te-particles per  $\text{cm}^3$ . The size distribution data indicated a log-normal distribution with peaks at 1.6, 7, and 12- $\mu\text{m}$  in diameter. The largest size class Te-particles, denoted as  $r_3$ , were clearly tetrahedrons faceted along (111)-type planes with edges along  $\langle 110 \rangle$ -type directions. The smallest size class of Te-particles, denoted as  $r_1$ , was distributed log-normal and was strongly positively correlated at small distances from the analysis of their corresponding pair correlation function. These  $r_1$  particles were negatively correlated with the  $r_3$  Te-particles. The  $r_1$  Te-particles were also observed to be patterned at a higher level by being generally arranged in a cellular structure consisting of planar arrangements lying along (111) planes in the CZT matrix and having a linear separation distance of about 145  $\mu\text{m}$  as determined by a Fourier transform image analysis.

The intermediate size class,  $r_2$ , was not strongly correlated with  $r_3$  but were present in string-of-pearl arrangements with  $r_1$  Te-particles and were considered to have formed due to a Rayleigh-Plateau instability of Te-rich solute trails during growth. Almost without exception the  $r_2$  size Te-particles lie along  $\langle 110 \rangle$ -type directions parallel to the growth direction, which was also close to  $\langle 110 \rangle$ , and on (111)-type planes. These linear  $r_2$  features were also observed to be separated by distances on the order of 200  $\mu\text{m}$  where they appeared. It was considered that these linear features were indicative of more severe growth instabilities compared to the majority of the as-grown boule that was studied. The  $r_2$  size Te-particles were more likely to form near the growth tip and near the growth heel. However,  $r_1$  size  $\langle 110 \rangle$ -type linear growth features were observed throughout the boule. Several grain and twin boundaries were imaged, but not carefully analyzed, and were observed to contain a large density of  $r_2$  size Te-particles lying in the plane of each type of defect.

A careful analysis of the growth features from the Te-particle spatial distributions, coupled with images from several small crucible growth experiments with  $\text{Cd}_{30}\text{Te}_{70}$  starting compositions, indicated that all of the growth features observed here could be explained by constitutional supercooling during growth leading to growth instabilities and cellular growth structures. Te-particles and Te-rich regions were likely entrained during growth leading to the observed Te-particle distributions. In short, this CZT boule, which was grown unseeded, was grown too fast and solid-liquid growth instabilities dominated the

solidification process and determined the resulting Te-particle distributions. The analysis here was thorough and the Te-particle data set was large enough to serve as a signature of what constitutional supercooling looks like in large single crystals of CZT. It is hoped that such a dataset can aid others trying to grow large, perfect single crystals of CZT. This study, and others, point to seeded growth and careful control of melt stoichiometry, perhaps using crucible rotation and melt stirring, to control and prevent these types of growth instabilities.

## 6. References

1. Sundaram, S.K., C.H. Henager Jr, D.J. Edwards, A.L. Schemer-Kohn, M. Bliss, and B.R. Riley, "Electron backscatter diffraction analysis of a CZT growth tip from a vertical gradient freeze furnace," *Journal of Crystal Growth*, 2011, 329(1), 12-19.
2. Roy, U.N., S. Weiler, J. Stein, A. Hossain, G.S. Camarda, A.E. Bolotnikov, and R.B. James, "Size and distribution of Te inclusions in THM as-grown CZT wafers: The effect of the rate of crystal cooling," *Journal of Crystal Growth*, 2011, 332(1), 34-38.
3. Awadalla, S.A., J. Mackenzie, H. Chen, B. Redden, G. Bindley, M.C. Duff, A. Burger, M. Groza, V. Buliga, J.P. Bradley, Z.R. Dai, N. Teslich, and D.R. Black, "Characterization of detector-grade CdZnTe crystals grown by traveling heater method (THM)," *Journal of Crystal Growth*, 2010, 312(4), 507-513.
4. Henager Jr, C.H., D.J. Edwards, A.L. Schemer-Kohn, M. Bliss, and J.E. Jaffe, "Preferential orientation of Te particles in melt-grown CZT," *Journal of Crystal Growth*, 2009, 311(9), 2641-2647.
5. Chen, H., S.A. Awadalla, K. Iniewski, P.H. Lu, F. Harris, J. MacKenzie, T. Hasanen, W. Chen, R. Redden, G. Bindley, I. Kuvvetli, C. Budtz-Jorgensen, P. Luke, M. Amman, J.S. Lee, A.E. Bolotnikov, G.S. Camarda, Y. Cui, A. Hossain, and R.B. James, "Characterization of large cadmium zinc telluride crystals grown by traveling heater method," *Journal of Applied Physics*, 2008, 103(1), 014903.
6. Mandal, K.C., S.H. Kang, M. Choi, A. Kargar, M.J. Harrison, D.S. McGregor, A.E. Bolotnikov, G.A. Carini, G.C. Camarda, and R.B. James, "Characterization of low-defect Cd<sub>0.9</sub>Zn<sub>0.1</sub>Te and CdTe crystals for high-performance frisch collar detectors," *IEEE Transactions on Nuclear Science*, 2007, 54(4), 802-806.
7. Chen, H., S.A. Awadalla, J. Mackenzie, R. Redden, G. Bindley, A.E. Bolotnikov, G.S. Camarda, G. Carini, and R.B. James, "Characterization of Traveling Heater Method (THM) grown Cd<sub>0.9</sub>Zn<sub>0.1</sub>Te crystals," *IEEE Transactions on Nuclear Science*, 2007, 54(4), 811-816.
8. Carini, G.A., A.E. Bolotnikov, G.S. Camarda, and R.B. James, "High-resolution X-ray mapping of CdZnTe detectors," *Nuclear Instruments and Methods in Physics Research, Section A: Accelerators, Spectrometers, Detectors and Associated Equipment*, 2007, 579(1), 120-124.
9. Bolotnikov, A.E., G.S. Camarda, G.A. Carini, Y. Cui, L. Li, and R.B. James, "Cumulative effects of Te precipitates in CdZnTe radiation detectors," *Nuclear Instruments and Methods in Physics*

- Research, Section A: Accelerators, Spectrometers, Detectors and Associated Equipment, 2007, 571(3), 687-698.
10. Bolotnikov, A.E., G.S. Camarda, G.A. Carini, Y. Cui, L. Li, and R.B. James, "Modelling the effects of Te precipitates on the electron transport in CdZnTe radiation detectors," Nuclear Instruments and Methods in Physics Research, Section A: Accelerators, Spectrometers, Detectors and Associated Equipment, 2007, 579(1), 125-129.
  11. Bolotnikov, A.E., G.S. Camarda, G.A. Carini, Y. Cui, K.T. Kohman, L. Li, M.B. Salomon, and R.B. James, "Performance-limiting defects in CdZnTe detectors," IEEE Transactions on Nuclear Science, 2007, 54(4), 821-827.
  12. Mandal, K.C., S.H. Kang, M. Choi, J. Bello, L. Zheng, H. Zhang, M. Groza, U.N. Roy, A. Burger, G.E. Jellison, D.E. Holcomb, G.W. Wright, and J.A. Williams, "Simulation, modeling, and crystal growth of Cd<sub>0.9</sub>Zn<sub>0.1</sub>Te for nuclear spectrometers," Journal of Electronic Materials, 2006, 35(6), 1251-1256.
  13. Cui, Y., M. Groza, G.W. Wright, U.N. Roy, A. Burger, L. Li, F. Lu, M.A. Black, and R.B. James, "Characterization of Cd<sub>1-x</sub>Zn<sub>x</sub>Te crystals grown from a modified vertical bridgman technique," Journal of Electronic Materials, 2006, 35(6), 1267-1274.
  14. Carini, G.A., A.E. Bolotnikov, G.S. Camarda, G.W. Wright, R.B. James, and L. Li, "Effect of Te precipitates on the performance of CdZnTe detectors," Applied Physics Letters, 2006, 88(14), 143515.
  15. Bolotnikov, A.E., G.S. Camarda, G.A. Carini, G.W. Wright, L. Li, A. Burger, M. Groza, and R.B. James, "Large area/volume CZT nuclear detectors," Physica Status Solidi C: Conferences, 2005, 2(5), 1495.
  16. Sang, W., Y. Qian, W. Shi, L. Wang, J. Yang, and D. Liu, "Equilibrium partial pressures and crystal growth of Cd<sub>1-x</sub>Zn<sub>x</sub>Te," Journal of Crystal Growth, 2000, 214, 30-34.
  17. MacKenzie, J., H. Chen, S.A. Awadalla, P. Marthandam, R. Redden, G. Bindley, Z. He, D.R. Black, M. Duff, M. Amman, J.S. Lee, P.N. Luke, M. Groza, and A. Burger, "Recent advances in THM CZT for nuclear radiation detection," in 2009 MRS Spring Meeting, April 14, 2009 - April 16, 2009, 2010, San Francisco, CA, United states: Materials Research Society.
  18. Chen, H., S.A. Awadalla, R. Redden, G. Bindley, A.E. Bolotnikov, G.S. Camarda, G. Carini, and R.B. James, "High-performance, large-volume THM CdZnTe detectors for medical imaging and homeland security applications," in 2006 IEEE Nuclear Science Symposium Conference Record, 29 Oct.-4 Nov. 2006, 2007, Piscataway, NJ, USA: IEEE.

19. Mengesha, W., C.E. Aalseth, D.S. Barnett, M. Bliss, and C. Schaefer, "Pulse shape analysis for electron mobility study in cadmium zinc telluride gamma-ray detectors," *IEEE Transactions on Nuclear Science*, 2004, 51(3), 1166-71.
20. Burger, A., M. Groza, Y. Cui, D. Hillman, E. Brewer, A. Bilikiss, G.W. Wright, L. Li, F. Lu, and R.B. James, "Characterization of large single-crystal gamma-ray detectors of cadmium zinc telluride," *Journal of Electronic Materials*, 2003, 32(7), 756.
21. Schieber, M., T.E. Schlesinger, R.B. James, H. Hermon, H. Yoon, and M. Goorsky, "Study of impurity segregation, crystallinity, and detector performance of melt-grown cadmium zinc telluride crystals," *Journal of Crystal Growth*, 2002, 237-239(1-4 III), 2082-2090.
22. Brunett, B.A., J.M. Van Scyoc, N.R. Hilton, J.C. Lund, and R.B. James, "Performance effects of crystal boundaries in cadmium zinc telluride radiation spectrometers," *IEEE Transactions on Nuclear Science*, 2000, 47(4 I), 1353-1359.
23. Lund, J.C., J.M. VanScyoc, III, R.B. James, D.S. McGregor, and R.W. Olsen, "Large volume room temperature gamma-ray spectrometers from Cd<sub>x</sub>Zn<sub>1-x</sub>Te," *Nuclear Instruments & Methods in Physics Research, Section A: Accelerators, Spectrometers, Detectors and Associated Equipment*, 1996, 380(1-2), 256.
24. Zhang, F., C. Herman, Z. He, G. De Geronimo, E. Vernon, and J. Fried, "Characterization of the H3D ASIC readout system and 6.0 cm<sup>3</sup> 3-D position sensitive CdZnTe detectors," *IEEE Transactions on Nuclear Science*, 2012, 59(1 PART 2), 236-242.
25. Li, Q., M. Beilicke, K. Lee, A. Garson Iii, Q. Guo, J. Martin, Y. Yin, P. Dowkontt, G. De Geronimo, I. Jung, and H. Krawczynski, "Study of thick CZT detectors for X-ray and Gamma-ray astronomy," *Astroparticle Physics*, 2011, 34(10), 769-777.
26. Vernon, E., K. Ackley, G. De Geronimo, J. Fried, Z. He, C. Herman, and F. Zhang, "ASIC for high rate 3D position sensitive detectors," *IEEE Transactions on Nuclear Science*, 2010, 57(3 PART 3), 1536-1542.
27. Martin, J., O. Schulz, T. Neddermann, T. Koettig, M. Beilicke, A. Garson, Q. Guo, K. Lee, Q. Li, and H. Krawczynski, "Results from operating pixelated CZT at low-background for the COBRA experiment," in *2010 IEEE Nuclear Science Symposium, Medical Imaging Conference, NSS/MIC 2010 and 17th International Workshop on Room-Temperature Semiconductor X-ray and Gamma-ray Detectors, RTSD 2010*, October 30, 2010 - November 6, 2010, 2010, Knoxville, TN, United states: Institute of Electrical and Electronics Engineers Inc.
28. Lee, K., J.W. Martin, A.B. Garson Iii, M. Beilicke, Q. Guo, Q. Li, G. De Geronimo, M. Groza, A. Burger, and H. Krawczynski, "Development of X-ray and gamma-ray CZT detectors for

- Homeland Security Applications," in Detection and Sensing of Mines, Explosive Objects, and Obscured Targets XV, April 5, 2010 - April 9, 2010, 2010, Orlando, FL, United states: SPIE.
29. Kuvvetli, I., C. Budtz-Jrgensen, E. Caroli, and N. Auricchio, "CZT drift strip detectors for high energy astrophysics," Nuclear Instruments and Methods in Physics Research, Section A: Accelerators, Spectrometers, Detectors and Associated Equipment, 2010, 624(2), 486-491.
  30. Auricchio, N., A. Basili, E. Caroli, C. Budtz-Jorgensen, R.M.C. Da Silva, S. Del Sordo, I. Kuvvetli, A. Mangano, L. Milano, L. Natalucci, E.M. Quadrini, J.B. Stephen, M. Zanichelli, and A. Zappettini, "A CZT high efficiency detector with 3D spatial resolution for Laue lens applications," in 2010 IEEE Nuclear Science Symposium, Medical Imaging Conference, NSS/MIC 2010 and 17th International Workshop on Room-Temperature Semiconductor X-ray and Gamma-ray Detectors, RTSD 2010, October 30, 2010 - November 6, 2010, 2010, Knoxville, TN, United states: Institute of Electrical and Electronics Engineers Inc.
  31. Kim, J., B. Donmez, K. Nelson, and Z. He, "Three-dimensional signal correction on UltraPeRL CZT detectors," in 2007 IEEE Nuclear Science Symposium and Medical Imaging Conference, NSS-MIC, October 27, 2007 - November 3, 2007, 2007, Honolulu, HI, United states: Institute of Electrical and Electronics Engineers Inc.
  32. Chen, H., S.A. Awadalla, K. Iniewski, P.H. Lu, F. Harris, J. Mackenzie, T. Hasanen, W. Chen, R. Redden, G. Bindley, I. Kuvvetli, C. Budtz-Jrgensen, P. Luke, M. Amman, J.S. Lee, A.E. Bolotnikov, G.S. Camarda, Y. Cui, A. Hossain, and R.B. James, "Large-volume, high-resolution cadmium zinc telluride radiation detectors: Recent developments," in Hard X-Ray and Gamma-Ray Detector Physics IX, August 27, 2007 - August 29, 2007, 2007, San Diego, CA, United states: SPIE.
  33. Camarda, G.S., A.E. Bolotnikov, Y. Cui, A. Hossain, K.T. Kohman, and R.B. James, "CdZnTe room-temperature semiconductor gamma-ray detector for national-security applications," in 2007 IEEE Long Island Systems, Applications and Technology Conference, LISAT, May 4, 2007 - May 4, 2007, 2007, Farmingdale, NY, United states: Inst. of Elec. and Elec. Eng. Computer Society.
  34. Zhang, F., Z. He, G.F. Knoll, D.K. Wehe, and J.E. Berry, "3D position sensitive CdZnTe spectrometer performance using third generation VAS/TAT readout electronics," in 2004 Nuclear Science Symposium, Medical Imaging Conference, Symposium on Nuclear Power Systems and the 14th International Workshop on Room Temperature Semiconductor X- and Gamma- Ray Detectors, October 16, 2004 - October 22, 2004, 2004, Rome, Italy: Institute of Electrical and Electronics Engineers Inc.

35. Zhang, F. and Z. He, "3D position sensitive CdZnTe gamma-ray spectrometers - Improved performance with new ASICs," in *Hard X-Ray and Gamma-Ray Detector Physics VI*, August 2, 2004 - August 3, 2004, 2004, Denver, CO, United states: SPIE.
36. Narita, T., J.E. Grindlay, J. Hong, and F.C. Niestemski, "Anode Readout for Pixellated CZT Detectors," in *X-Ray and Gamma-Ray Instrumentation for Astronomy XIII*, August 3, 2003 - August 5, 2003, 2004, San Diego, CA, United states: SPIE.
37. Kakuno, E.M., G.S. Camarda, and D.P. Siddons, "Cadmium-zinc telluride detector arrays for synchrotron radiation applications," *Proceedings of SPIE-The International Society for Optical Engineering*, 2004, 5198(*Hard X-Ray and Gamma-Ray Detector Physics V*), 19-25.
38. Zhang, F., Z. He, and D. Xu, "Analysis of detector response using 3-D position sensitive CZT gamma-ray spectrometers," in *2003 IEEE Nuclear Science Symposium Conference Record - Nuclear Science Symposium, Medical Imaging Conference*, October 19, 2003 - October 25, 2003, 2003, Portland, OR, United states: Institute of Electrical and Electronics Engineers Inc.
39. Bolotnikov, A.E., M. Black, G.S. Camarda, G.A. Carini, Y. Cui, K.T. Kohman, L. Li, M.B. Salomon, and R.B. James, "The effect of Te precipitates on characteristics of CdZnTe detectors," in *Hard X-Ray and Gamma-Ray Detector Physics and Penetrating Radiation Systems VIII*, 2006, Bellingham WA, WA 98227-0010, United States: International Society for Optical Engineering.
40. Triboulet, R. and P. Siffert, eds. "CdTe and Related Compounds; Physics, Defects, Hetero- and Nano-structures, Crystal Growth, Surfaces and Applications," *European Materials Research Society Monographs*, Vol. 1, 2010, Elsevier Ltd., 296.
41. Ndap, J.-O., "Inclusions and Precipitates in CdZnTe Substrates," in *CdTe and Related Compounds; Physics, Defects, Hetero- and Nano-structures, Crystal Growth, Surfaces and Applications*, Vol. 1, R. Triboulet and P. Siffert, Editors, 2010, Elsevier Ltd., p. 228-257.
42. Durose, K., "Extended Defects in CdTe" in *CdTe and Related Compounds; Physics, Defects, Hetero- and Nano-structures, Crystal Growth, Surfaces and Applications*, Vol. 1, R. Triboulet and P. Siffert, Editors, 2010, Elsevier Ltd., p. 171-227.
43. Rudolph, P., "Non-stoichiometry related defects at the melt growth of semiconductor compound crystals - A review," *Crystal Research and Technology*, 2003, 38(7-8), 542-554.
44. Rudolph, P., A. Engel, I. Schentke, and A. Grochocki, "Distribution and genesis of inclusions in CdTe and (Cd,Zn)Te single crystals grown by the Bridgman method and by the travelling heater method," *Journal of Crystal Growth*, 1995, 147(3-4), 297-304.

45. Rudolph, P., "Fundamental studies on Bridgman growth of CdTe," *Progress in Crystal Growth and Characterization of Materials*, 1994, 29(1-4), 275-381.
46. Rudolph, P. and M. Muhlberg, "Basic problems of vertical Bridgman growth of CdTe," *Mater. Sci. Eng. B*, 1993, B16(1-3), 8-16.
47. Muehlberg, M., P. Rudolph, C. Genzel, B. Wermke, and U. Becker, "Crystalline and chemical quality of CdTe and Cd<sub>1-x</sub>Zn<sub>x</sub>Te grown by the Bridgman method in low temperature gradients," *Journal of Crystal Growth*, 1990, 101(1-4), 275-280.
48. Rudolph, P., M. Neubert, and M. Muhlberg, "Defects in CdTe Bridgman monocrystals caused by nonstoichiometric growth conditions," *Journal of Crystal Growth*, 1993, 128(1-4 pt 2), 582-587.
49. Becker, U., H. Zimmermann, P. Rudolph, and R. Boyn, "Optical study of the impurity distribution in vertical-Bridgman-growth CdTe crystals," *Physica Status Solidi (A) Applied Research*, 1989, 112(2), 569-578.
50. Rai, R.S., S. Mahajan, S. McDevitt, and C.J. Johnson, "Characterization of CdTe, (Cd,Zn)Te, and Cd(Te,Se) single crystals by transmission electron microscopy," *J. Vac. Sci. Technol. B, Microelectron. Process. Phenom.*, 1991, 9(3), 1892-6.
51. Durose, K. and G.J. Russell, "Structural defects in CdTe crystals grown by two different vapour phase techniques," *J. Cryst. Growth*, 1988, 86(1-4), 471-6.
52. Chew, N.G., A.G. Cullis, and G.M. Williams, "Identification of tellurium precipitates in cadmium telluride layers grown by molecular beam epitaxy," *Applied Physics Letters*, 1984, 45(10), 1090-2.
53. Becker, U., P. Rudolph, R. Boyn, M. Wienecke, and I. Utke, "Characterization of p-type CdTe Bridgman crystals by infrared extinction spectra," *Physica Status Solidi (A) Applied Research*, 1990, 120(2), 653-660.
54. Aoyama, T., Y. Takamura, and K. Kuribayashi, "Dendrite growth processes of silicon and germanium from highly undercooled melts," *Metallurgical and Materials Transactions A: Physical Metallurgy and Materials Science*, 1999, 30(5), 1333-1339.
55. Davydov, A.A. and V.N. Maslov, "Theory of dendrite growth in germanium," *Kristallografiya*, 1964, 9(4), 472-476.
56. Bukhanova, A.A. and D.A. Petrov, "The growth of 110 dendrites in germanium," *Fizika Tverdogo Tela*, 1964, 6(8), 2520-2521.
57. Wagner, R.S., "On the growth of germanium dendrites," *Acta Metallurgica*, 1960, 8(1), 57-60.

58. Seidensticker, R.G., "Propagation mechanism of germanium dendrites," *Journal of Applied Physics*, 1960, 31(7), 1165-1168.
59. Bennett, A.I. and R.L. Longini, "Dendritic growth of germanium crystals," *Physical Review*, 1959, 116(1), 53-61.
60. Billig, E., "Growth of monocrystals of germanium from an undercooled melt," *Proceedings of the Royal Society of London, Series A (Mathematical and Physical Sciences)*, 1955, 229, 346-363.
61. Wang, T., W. Jie, and D. Zeng, "Observation of nano-scale Te precipitates in cadmium zinc telluride with HRTEM," *Materials Science and Engineering A*, 2008, 472(1-2), 227-230.
62. Espiau de Lamaestre, R. and H. Bernas, "Significance of lognormal nanocrystal size distributions," *Phys. Rev. B*, 2006, 73, 125317.
63. Bardsley, W., J.S. Boulton, and D.T.J. Hurle, "Constitutional supercooling during crystal growth from stirred melts. III. The morphology of the germanium cellular structure," *Solid-State Electronics*, 1962, 5, 395-403.
64. Hurle, D.T.J., "Constitutional supercooling during crystal growth from stirred melts. I. Theoretical," *Solid-State Electronics*, 1961, 3(1), 37-44.
65. Bardsley, W., J.M. Callan, H.A. Chedzey, and D.T.J. Hurle, "Constitutional supercooling during crystal growth from stirred melts. II. Experimental: gallium-doped germanium," *Solid-State Electronics*, 1961, 3(2), 142-154.
66. Tiller, W.A., K.A. Jackson, J.W. Rutter, and B. Chalmers, "The redistribution of solute atoms during the solidification of metals," *Acta Metallurgica*, 1953, 1(4), 428-437.
67. Szeles, C., W.C. Chalmers, S.E. Cameron, J.-O. Ndap, M. Bliss, and K.G. Lynn, "Semi-insulating CdZnTe with improved structural perfection for radiation detector applications," in *Hard X-Ray and Gamma-Ray Detector Physics III*, July 30, 2001 - August 1, 2001, 2001, San Diego, CA, United states: SPIE.
68. Yan, W., M. Jiahua, L. Xiaoyan, and C. Jun, "Investigation of effect of constitutional supercooling and solute segregation in CZT-LPVB with finite element analysis method," *Vacuum*, 2012, 86(7), 998-1002.
69. Hermon, H., M. Schieber, R.B. James, N. Yang, A.J. Antolak, D.H. Morse, N.N.P. Kolesnikov, Y.N. Ivanov, V. Komar, M.S. Goorsky, H. Yoon, J. Toney, and T.E. Schlesinger, "Comparison between cadmium zinc telluride crystals grown in Russia and in the Ukraine," in *Proceedings of the 1998 MRS Fall Symposium*, December 1, 1997 - December 5, 1997, 1998, Boston, MA, USA: MRS.

70. Vidal, J. and R. Romero, "Interface breakdown in heavily doped germanium single crystals grown from the melt," *Crystal Research and Technology*, 1981, 16(7), 853-9.
71. Bardsley, W., D.T.J. Jurle, M. Hart, and A.R. Lang, "Structural and chemical inhomogeneities in germanium single crystals grown under conditions of constitutional supercooling," *Journal of Crystal Growth*, 1980, 49(4), 612-30.
72. Bolotnikov, A.E., G.S. Camarda, Y. Cui, G. Yang, A. Hossain, K. Kim, and R.B. James, "Characterization and evaluation of extended defects in CZT crystals for gamma-ray detectors," *Journal of Crystal Growth*, 2013, 379, 46-56.
73. Marchini, L., A. Zappettini, M. Zha, N. Zambelli, A.E. Bolotnikov, G.S. Camarda, and R.B. James, "Crystal defects in CdZnTe crystals grown by the modified low-pressure Bridgman method," *IEEE Transactions on Nuclear Science*, 2012, 59(2), 264-267.
74. Hossain, A., L. Xu, A.E. Bolotnikov, G.S. Camarda, Y. Cui, G. Yang, K.H. Kim, and R.B. James, "Distribution of Te inclusions in a CdZnTe wafer and their effects on the electrical properties of fabricated devices," *Nuclear Instruments and Methods in Physics Research, Section A: Accelerators, Spectrometers, Detectors and Associated Equipment*, 2011, 652(1), 146-148.
75. Bolotnikov, A.E., S. Babalola, G.S. Camarda, Y. Cui, R. Gul, S.U. Egarievwe, P.M. Fochuk, M. Fuerstnau, J. Horace, A. Hossain, F. Jones, K.H. Kim, O.V. Kopach, B. McCall, L. Marchini, B. Raghathamachar, R. Taggart, G. Yang, L. Xu, and R.B. James, "Correlations Between Crystal Defects and Performance of CdZnTe Detectors," *IEEE Transactions on Nuclear Science*, 2011, 58(4), 1972-80.
76. Billig, E. and P.J. Holmes, "Some observations on growth and etching of crystals with the diamond or zincblende structure," *Acta Crystallographica*, 1955, 8, 353-354.
77. Xu, L., W. Jie, A.E. Bolotnikov, U.N. Roy, J. Stein, A. Hossain, G.S. Camarda, K.H. Kim, G. Yang, R. Gul, Y. Cui, Y. Xu, T. Wang, G. Zha, and R.B. James, "Concentration of extended defects in CdZnTe single crystals: Effects of cooling rate after growth," *Journal of Crystal Growth*, 2012, 355(1), 84-87.
78. Fochuk, P., R. Grill, O. Kopach, A.E. Bolotnikov, E. Belas, M. Bugar, G. Camarda, W. Chan, Y. Cui, A. Hossain, K.H. Kim, I. Nakonechnyi, O. Panchuk, G. Yang, and R.B. James, "Elimination of Te inclusions in Cd<sub>1-x</sub>Zn<sub>x</sub>Te crystals by short-term thermal annealing," *IEEE Transactions on Nuclear Science*, 2012, 59(2), 256-263.
79. Rohrer, G.S., C.L. Rohrer, and W.W. Mullins, "Coarsening of faceted crystals," *Journal of the American Ceramic Society*, 2002, 85(3), 675-682.

80. Hagedorn, J.G., N.S. Martys, and J.F. Douglas, "Breakup of a fluid thread in a confined geometry: droplet-plug transition, perturbation sensitivity, and kinetic stabilization with confinement," *Physical Review E (Statistical, Nonlinear, and Soft Matter Physics)*, 2004, 69(5), 56312-1.
81. San Miguel, M., M. Grant, and J.D. Gunton, "Phase separation in two-dimensional binary fluids," *Physical Review A*, 1985, 31(2), 1001-1005.
82. Nichols, F.A. and W.W. Mullins, "Surface-(interface-) and volume-diffusion contributions to morphological changes driven by capillarity," *Transactions of the Metallurgical Society of Aime*, 1965, 233(10), 1840.
83. Thompson, C.V., "Solid-State Dewetting of Thin Films," *Annual Review of Materials Research*, 2012, 42(1), 399-434.

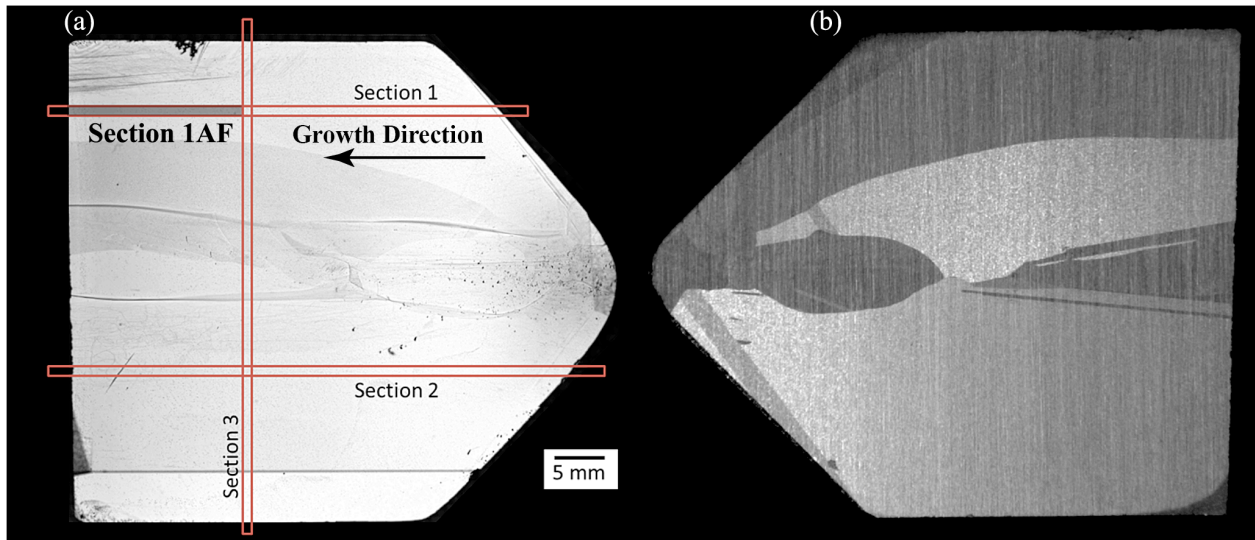
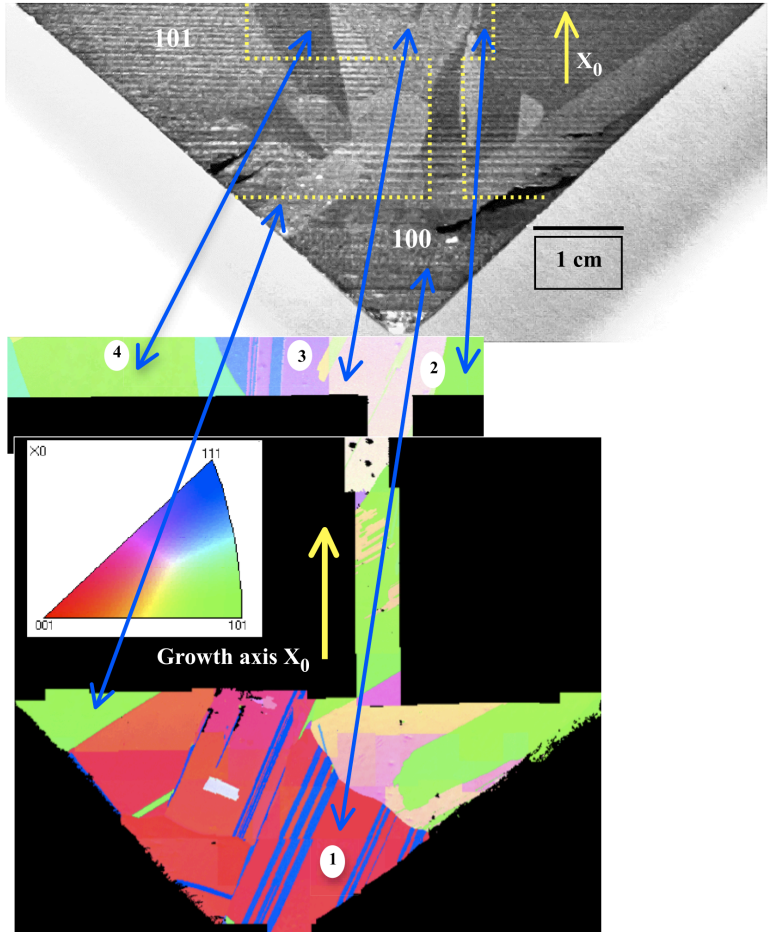
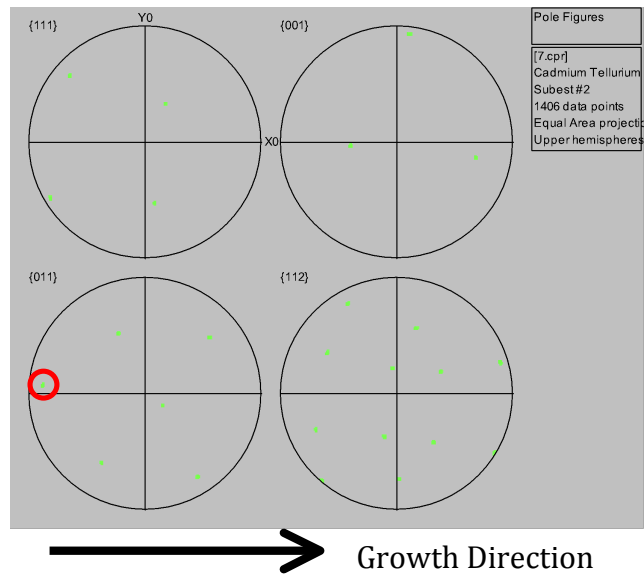


Figure 1. (a) TIR image of polished CZT section used for this study with the sections used for Te-particle analysis identified. (b) Optical image of the opposite half of the boule slice with a rough polish showing the individual grains. The shaded region in (a) is Section 1AF that is discussed later in the text.

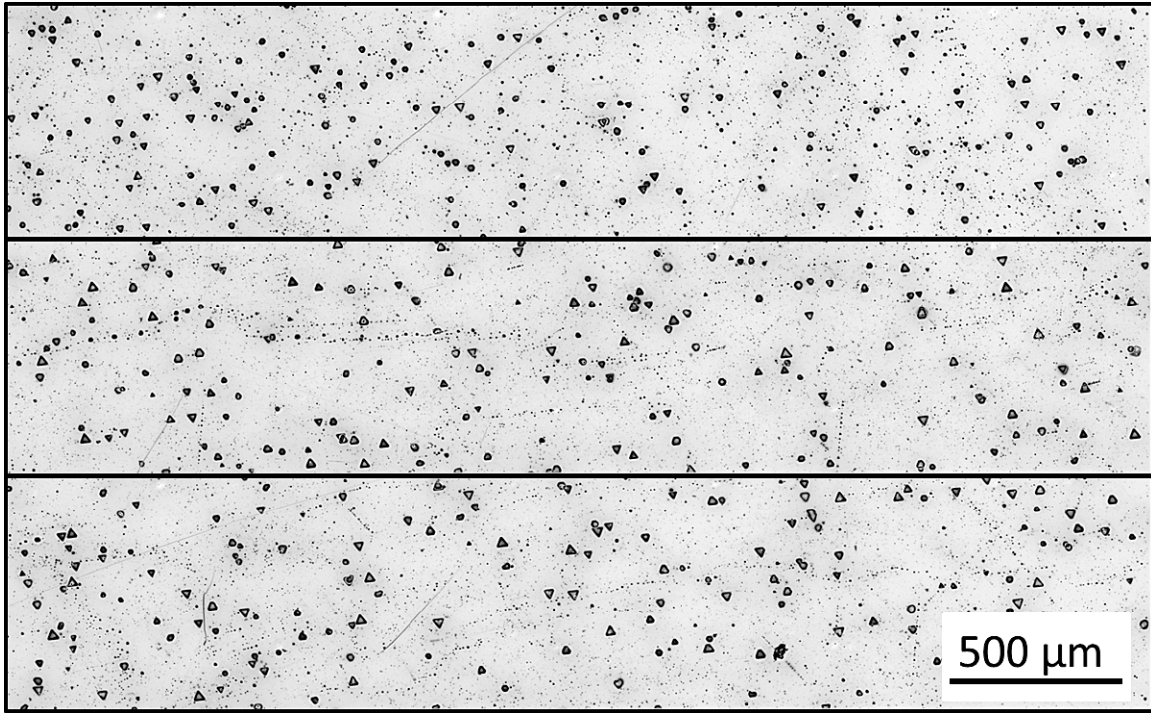


(a)

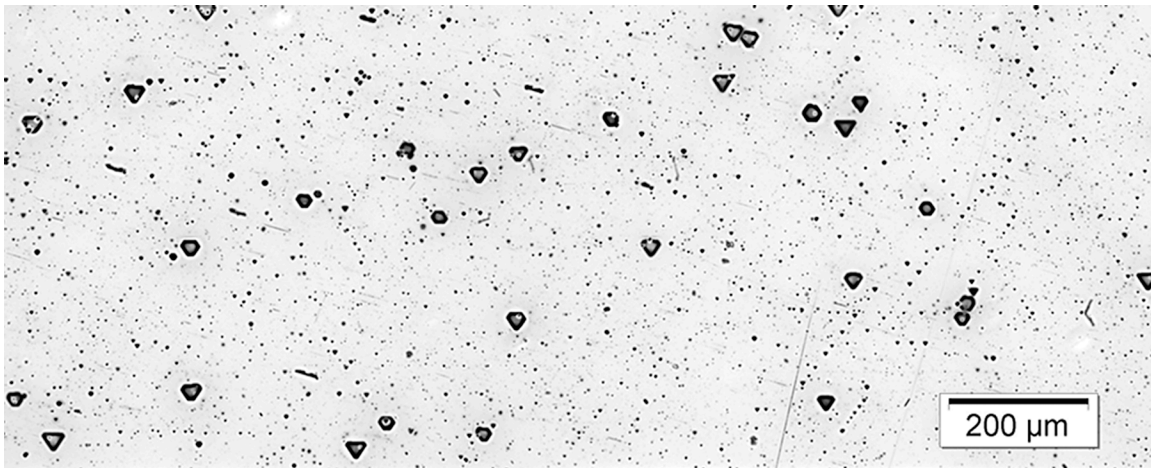


(b)

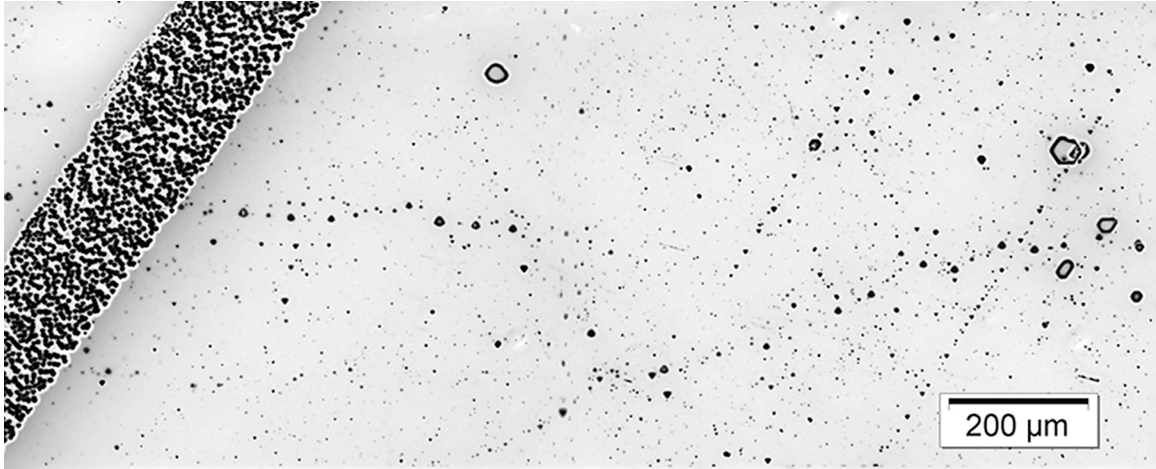
Figure 2. Electron beam backscatter diffraction (EBSD) data for the growth tip region of the CZT boule studied here. The grain indicated by 2 in (a) and colored light green is the grain orientation imaged in sections 1 and 2, and most of 3 as shown in Fig. 1. The coloring is the key to the inverse pole figure plot shown in the inset in (a). A pole figure plot for this orientation is shown in (b) showing the near  $\langle 110 \rangle$  growth axis (circled pole).



(a)



(b)



(c)

Figure 3: (a) Composite optical micrographs from three different locations along section 1. Note that these micrographs combine all of the z-slices into one image such that all particles appear to be in focus at the same time. The smaller Te-particles are seen to be relatively evenly dispersed, while the larger particle distributions exhibit more variation. Facets can also be clearly observed on the larger Te-particles. Images (b) and (c) show higher magnification images with faceted large particles and strings of smaller particles. A twin boundary in (c) on the left side of the image is highly decorated with Te-particles.

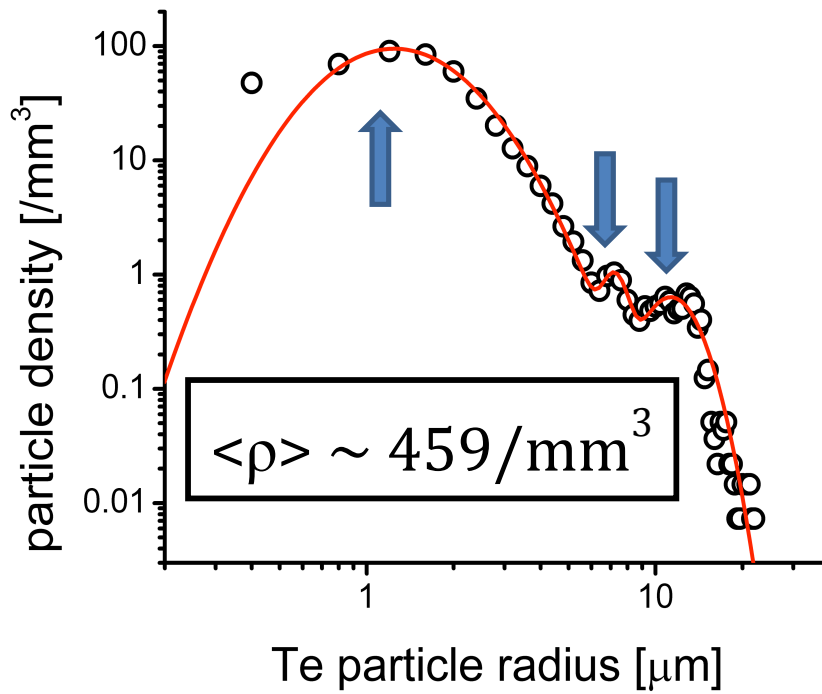


Figure 4: Average Te-particle size distribution along section 1 of the boule, along the growth axis. The data (open circles) has been fit (red solid line) with a tri-modal log-normal distribution. Peaks in the distribution occur at 1.6 μm, 7.3 μm, and 11.8 μm. Bimodal or higher complexity log-normal size distributions of Te-particles were observed to be typical in this sample.

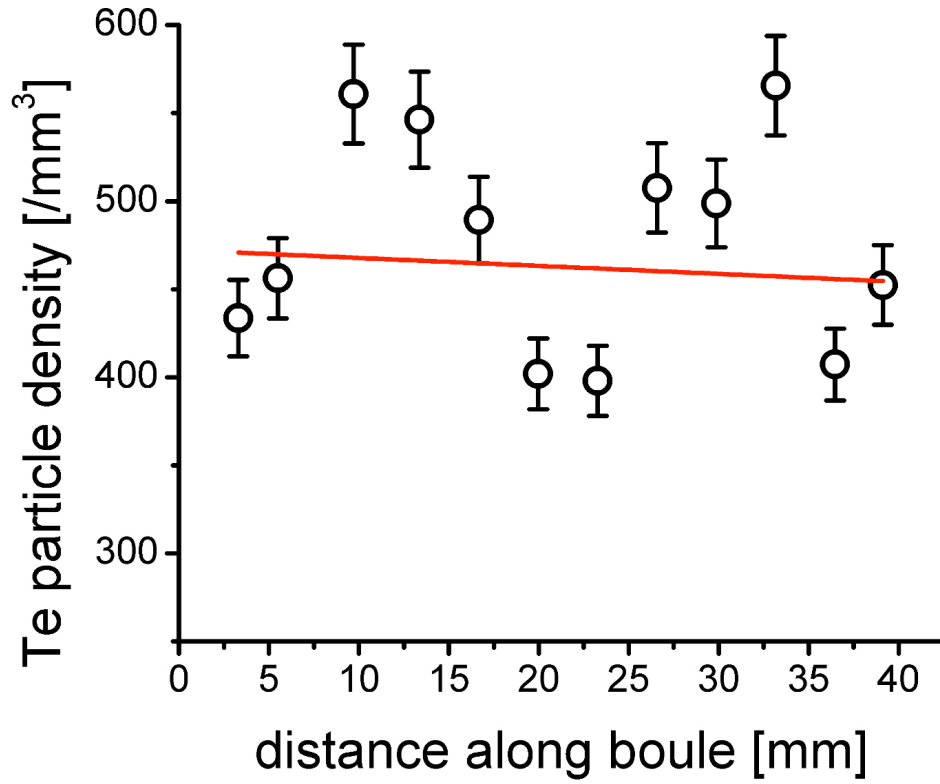
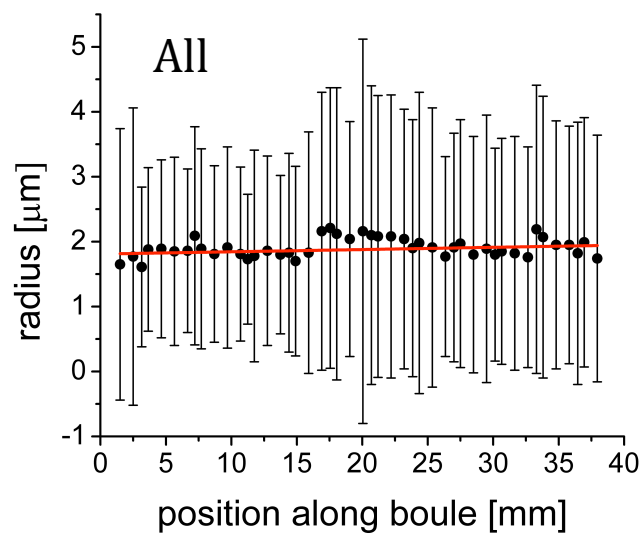
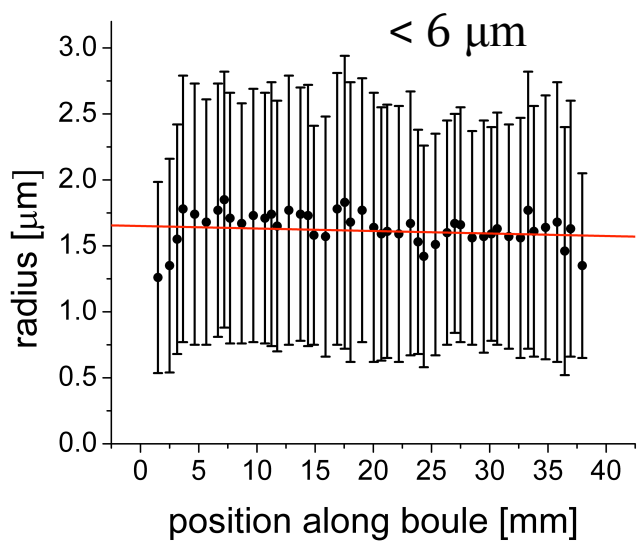


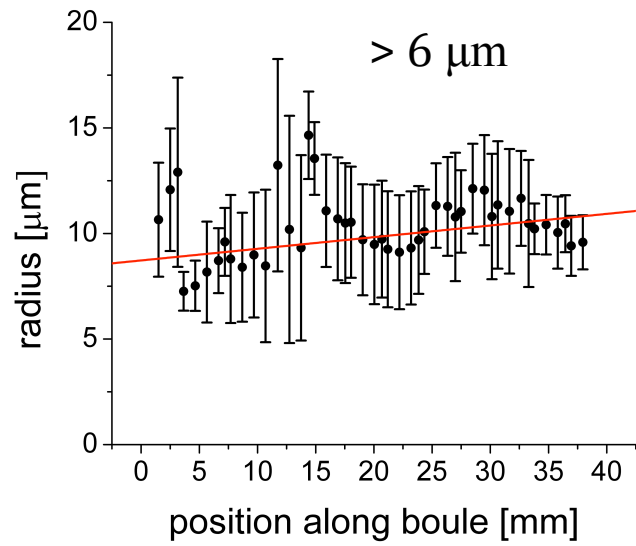
Figure 5. The variation in Te-particle density along the growth direction (referenced to Fig. 1) for Section 1 of the large CZT boule over a distance of about 40-mm in length.



(a)



(b)



(c)

Figure 6. These plots show (a) the total, (b) less than 6 μm, and (c) greater than 6 μm diameter Te-particles radii over a distance of about 40-mm in length. These data are referenced back to Fig. 1: Section 1.

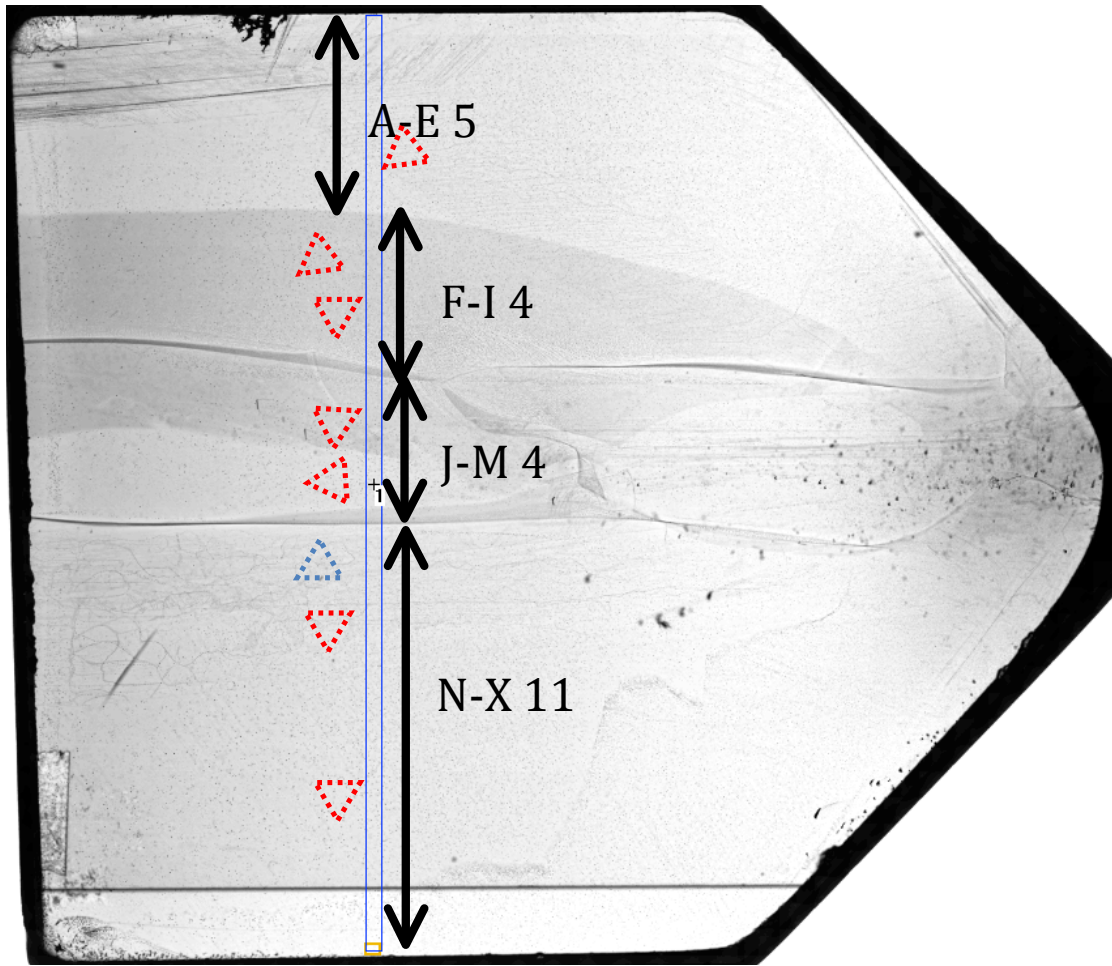


Figure 7. Schematic of Section 3 (radial section) with letter designations of regions of differing orientation denoted by the black arrows. The red and blue triangles denote the dominant orientation of the Te-particle tetrahedral, which will be detailed in the discussion.

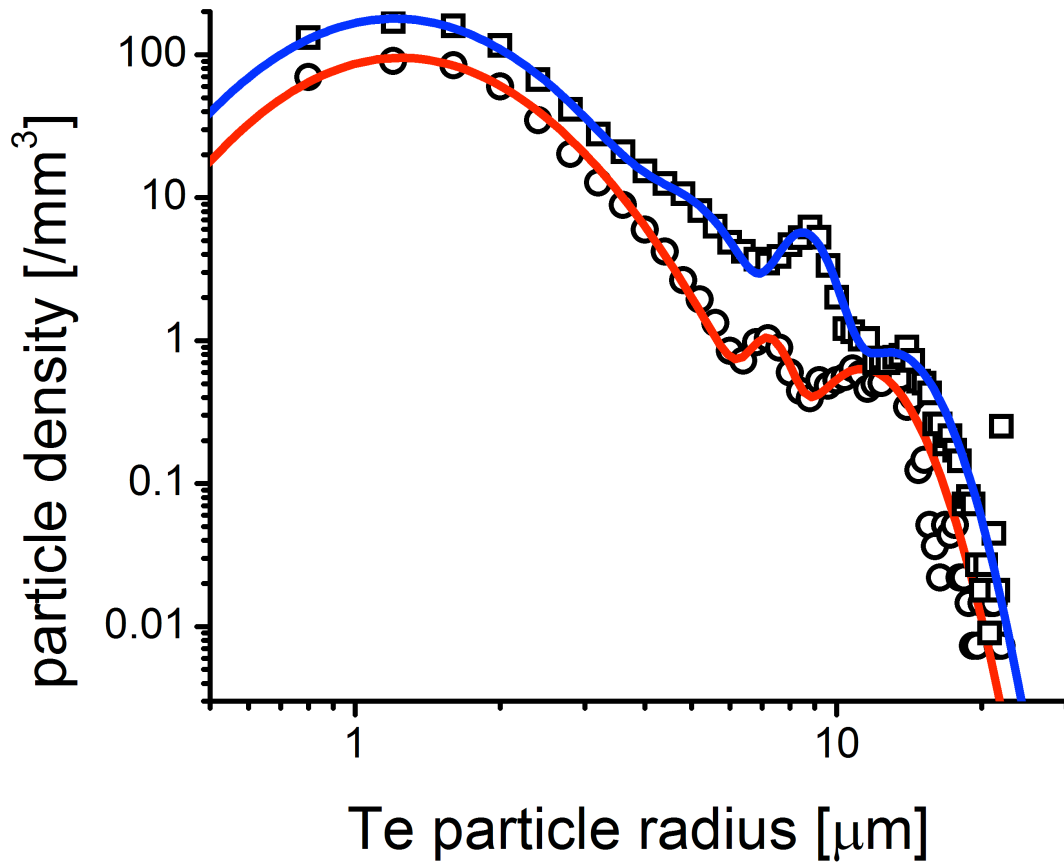
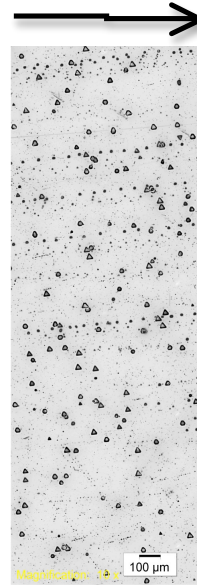
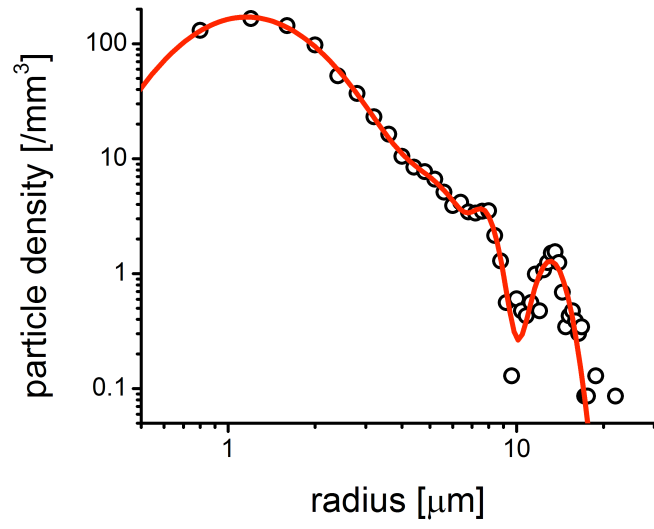
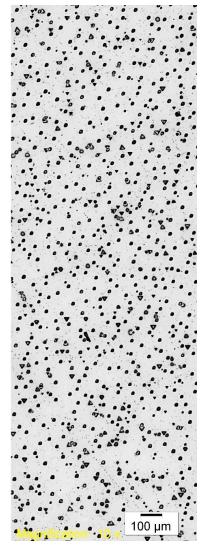
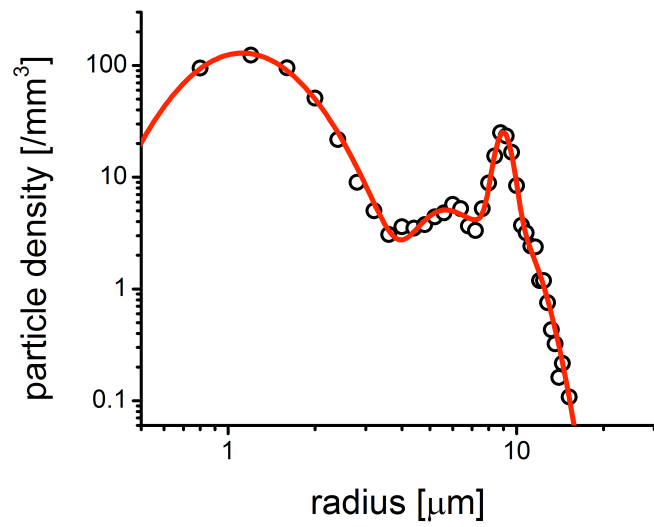


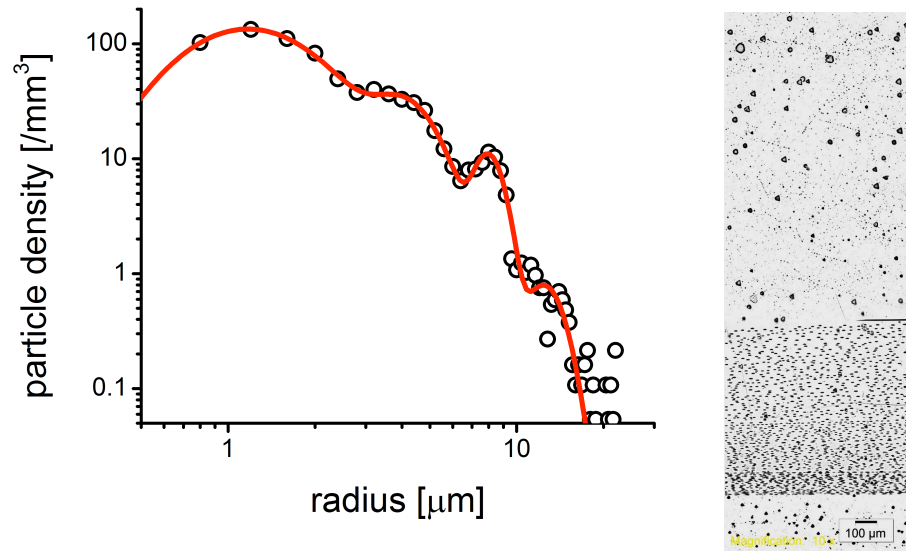
Figure 8. Particle density statistics along the radial Section 3 is shown in the blue curve (See Fig. 1), while the red curve shows the longitudinal distribution from Fig. 4. The radial data also indicates a multimodal Te-particle distribution with a slightly higher density and larger particle peak size.



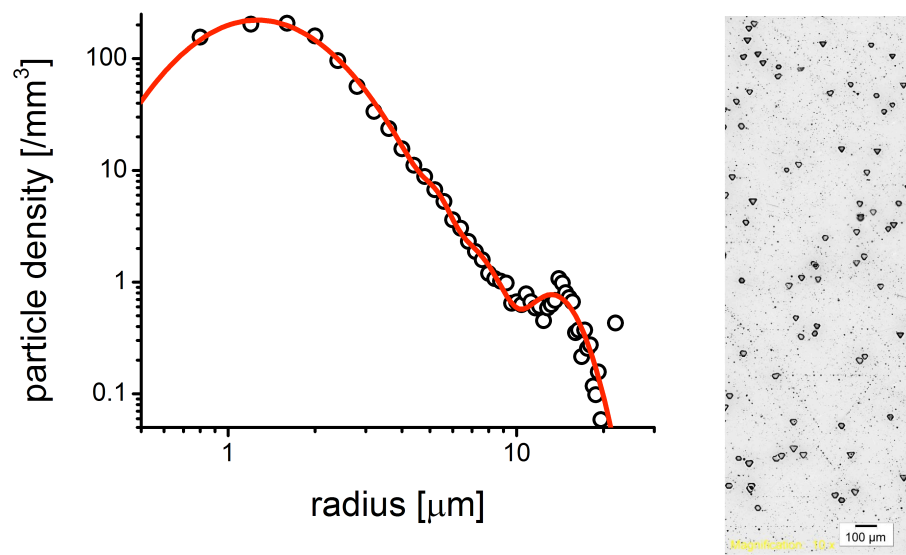
(a)



(b)



(c)



(d)

Figure 9. Log-normal plots of Te-particle distributions from the four separate grain regions shown in Fig. 7 in the radial direction together with representative TIR images from these regions.

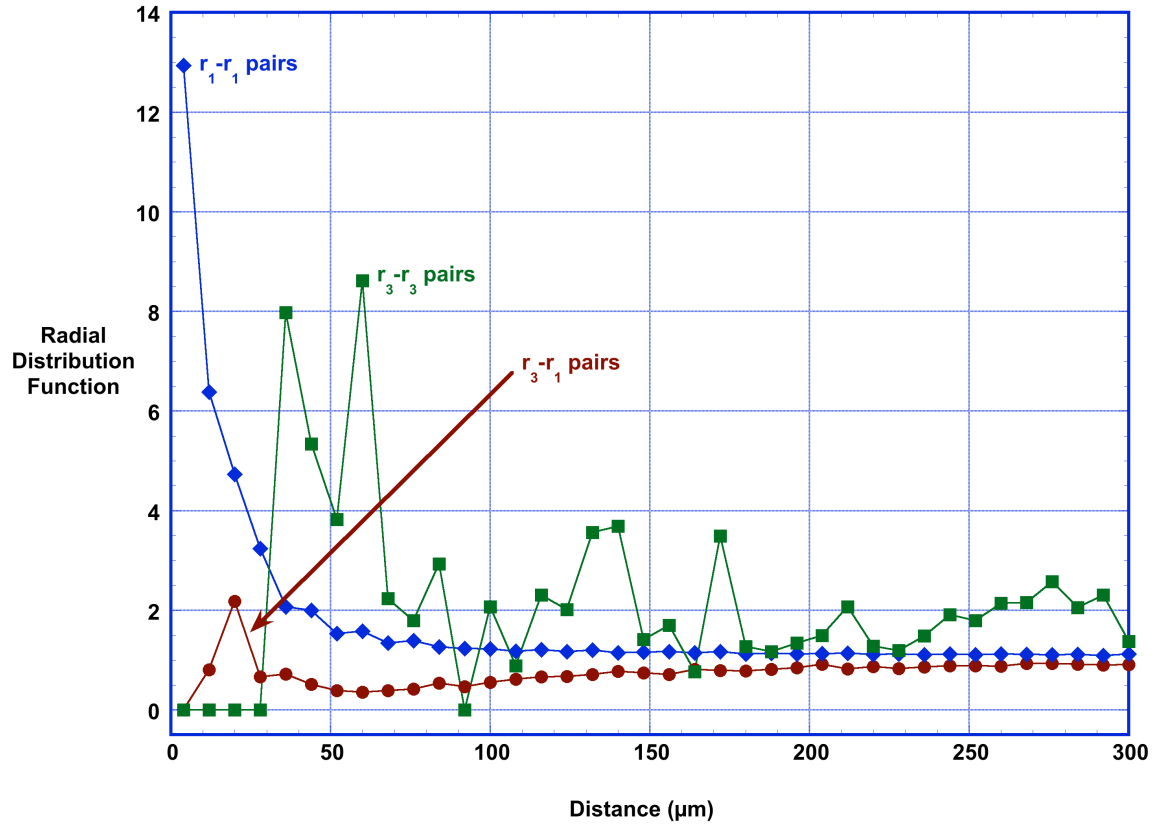
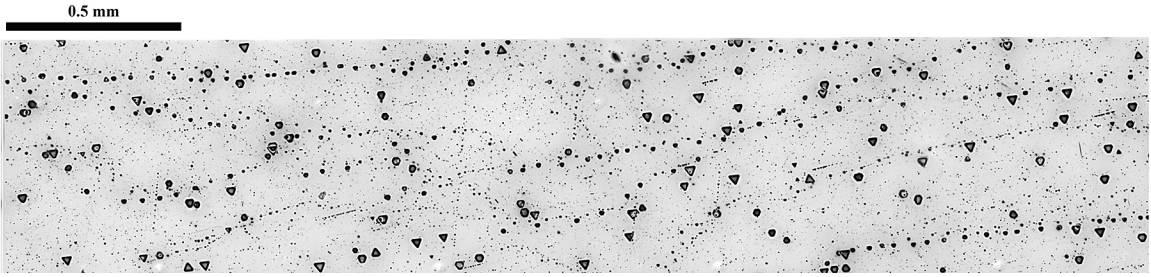
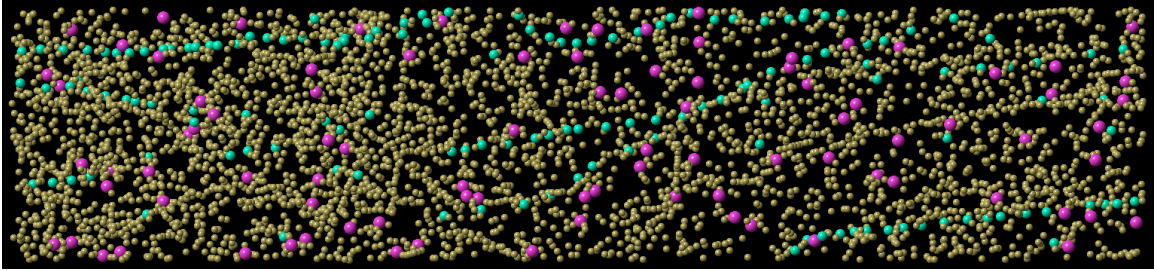


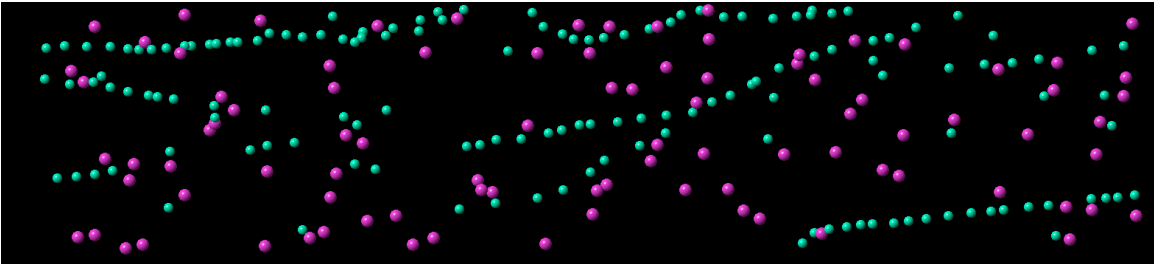
Figure 10. Radial distribution function (pair correlation) for volume 1AF containing almost 32,000 Te-particles. Shown are the  $r_1$  and  $r_3$  pair correlations with the  $r_2$  distribution excluded from the data.  $r_1$  is strongly correlated at small distances, while  $r_3$  is correlated at larger distances only. Of most significance, the  $r_1$ - $r_3$  pairs are negatively correlated out to almost 250  $\mu\text{m}$ . A zone denuded of the smallest particles surrounds each large Te-particle.



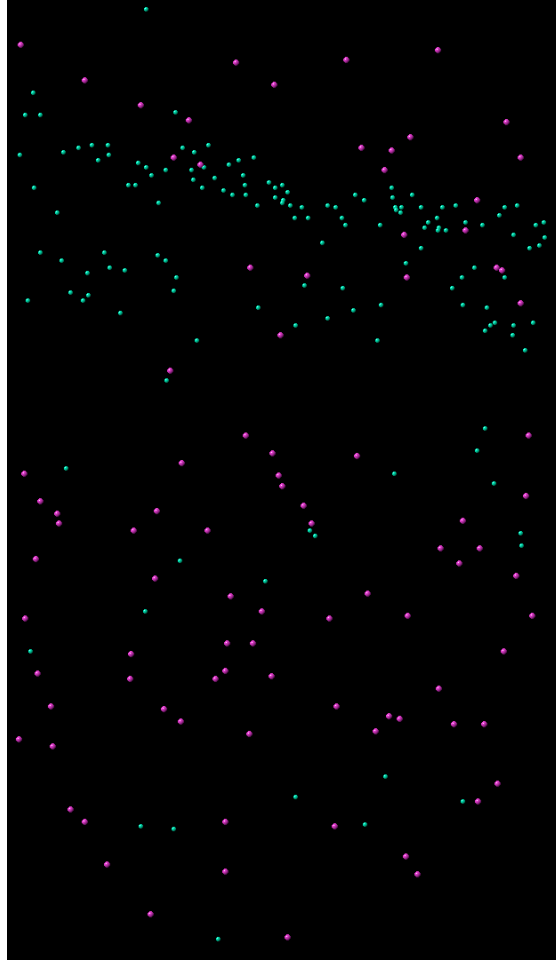
(a)



(b)

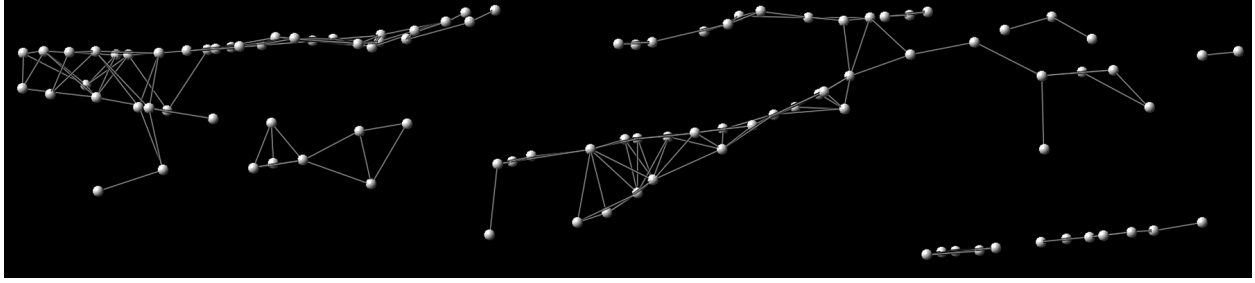


(c)



(d)

Figure 11. Volume element 1G viewed in different methods to illustrate Te-particle distributions (see text for details). The image in (a) shows the flattened TIR image with the growth direction horizontal from left to right in the image. Image in (b) is the same volume element but now the Te-particles are color coded with respect to size. Magenta is largest ( $r_3$ ), teal is  $r_2$ , and bronze is  $r_1$ , the smallest size class. The  $r_1$  particles are removed to create image (c), which emphasizes the linear features of the  $r_2$  Te-particles. The volume element is rotated  $90^\circ$  about the growth axis to create image (d) to reveal that the  $r_2$  size Te-particles are clustered in a local region of the volume.

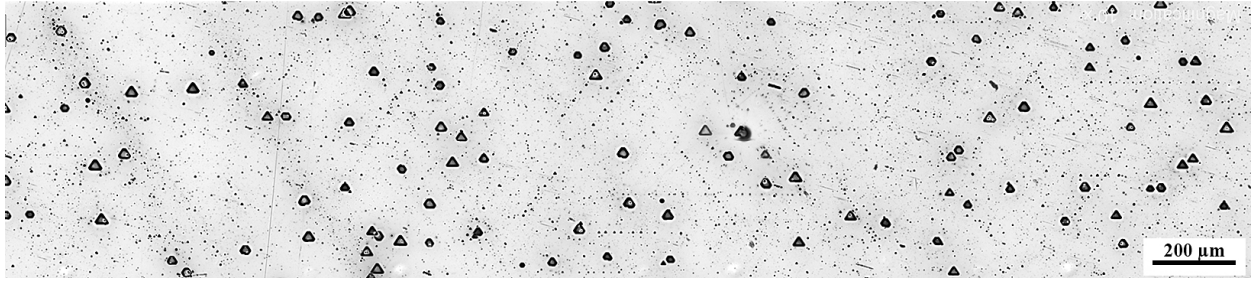


(a)

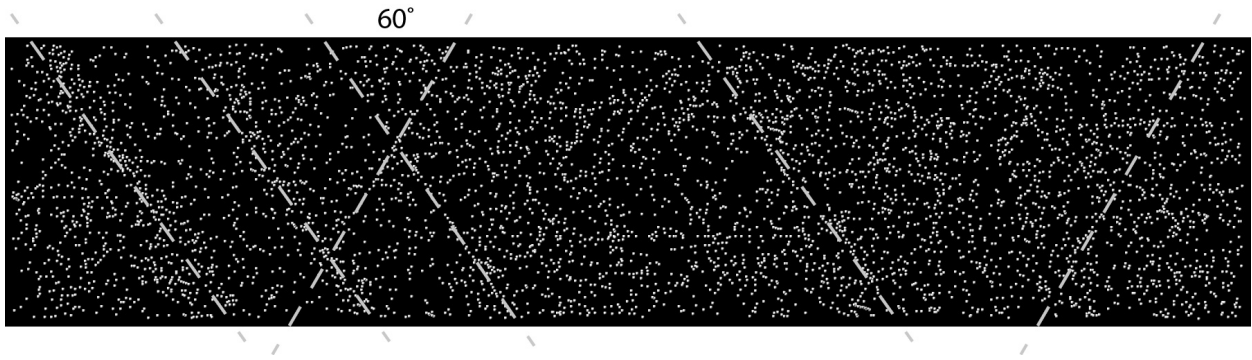


(b)

Figure 12. Intermediate size ( $r_2$  size class) Te-particles viewed from two perspectives from volume element 1G shown in Fig. 11. Image in (a) shows only the  $r_2$ -sized Te-particles that can be connected by bonds of length  $200\ \mu\text{m}$  or less. The image in (b) is created by rotating the volume element so that the  $\langle 110 \rangle$ -direction is normal to the page and is oriented edge on to a (111)-type plane. Thus, the  $r_2$ -size Te-particles lie along  $\langle 110 \rangle$ -type direction on a (111)-type plane in this volume in the CZT boule.



(a)

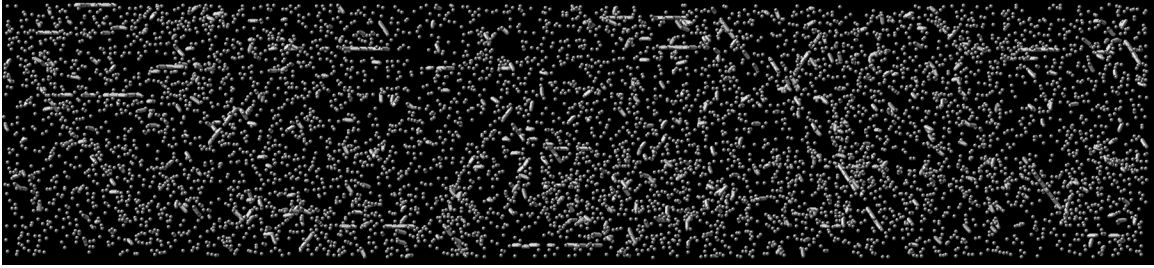


(b)



(c)

Figure 13. Smallest Te-particles aligned along  $\langle 110 \rangle$ -directions and on (111) planes in volume element 2I. Image in (a) is flattened TIR image, (b) is an image of  $r_1$  Te-particles enlarged with  $r_2$  and  $r_3$  not visible. The  $\langle 110 \rangle$ -type directions are indicated with the dashed lines. Shown in (c) is the model rotated to bring (111)-type planes into edge on view.



(a)



(b)

Figure 14. Aligned Te-particles and rotated view showing planar alignment as well. (a) is an image of  $r_1$  Te-particles enlarged with  $r_2$  and  $r_3$  not visible. Shown in (b) is the model rotated to bring (111)-type planes into edge on view.

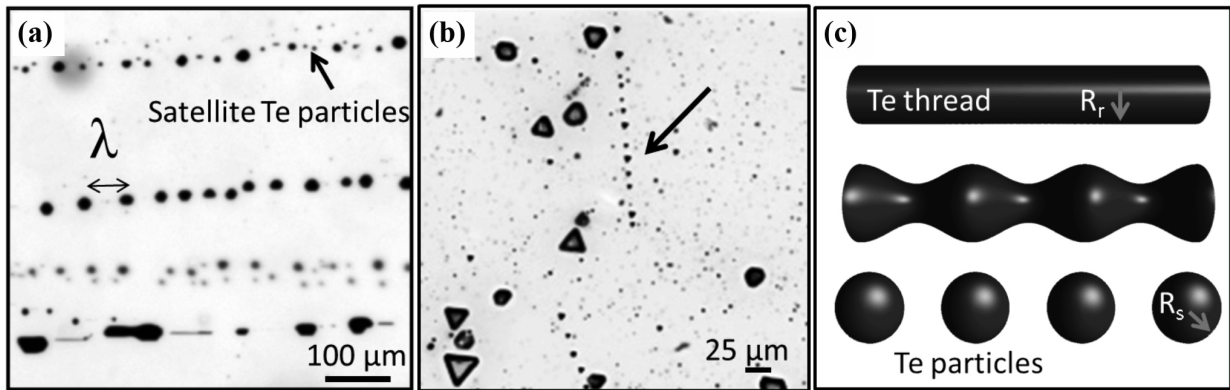
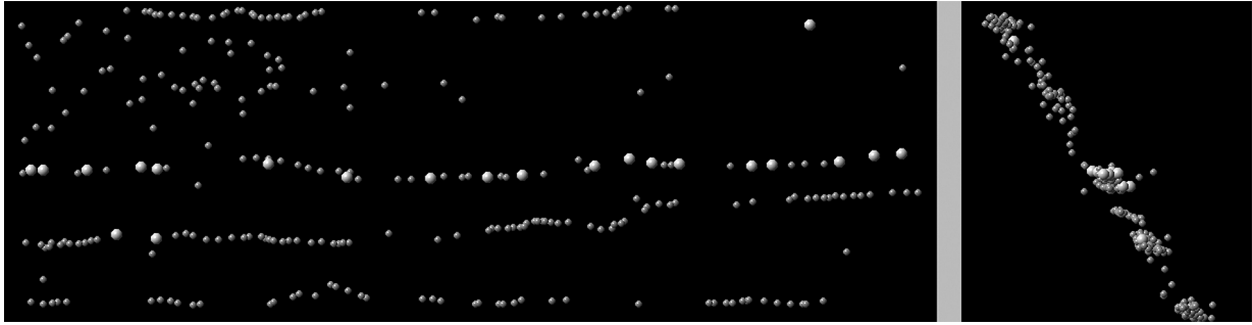


Figure 15. TIR image examples of quasi-periodic pearl-string formations within the boule. Shown in (a) are strings containing both  $r_1$  and  $r_2$ -sized Te-particles. Some of the strings have satellite  $r_1$  particles in between larger  $r_2$  particles. In the lower part of (a) solute trails are observed. These trails are not typical of this CZT boule. Shown in (c) is a schematic of a Rayleigh-Plateau thread break-up. The droplet wavelength observed here is consistent with this type of instability.



(a)

(b)

Figure 16. String-of-pearl image in volume element 2A near the growth heel with surrounding Te-particles removed to show the several collinear strings; one with clear satellite  $r_1$  Te-particles. The growth direction is left to right in (a). Shown in (b) is the same volume rotated to bring the (111)-type planes edge on in the view. Thus, all the strings lie along  $\langle 110 \rangle$ -type directions and on (1110)-type planes. Note the vertical spacing in (a) of several hundred microns.

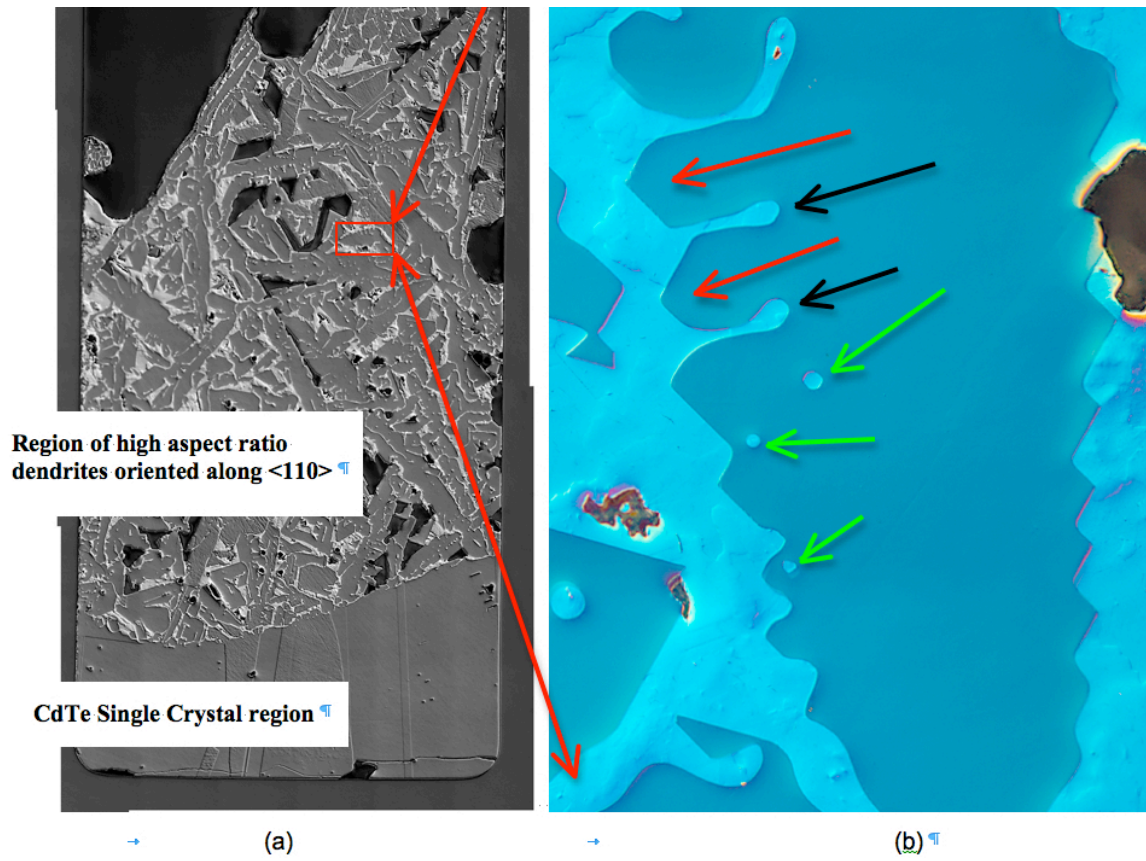


Figure 17. Small crucible growth experiment at 11K/min cooling rate showing CdTe growth instabilities.

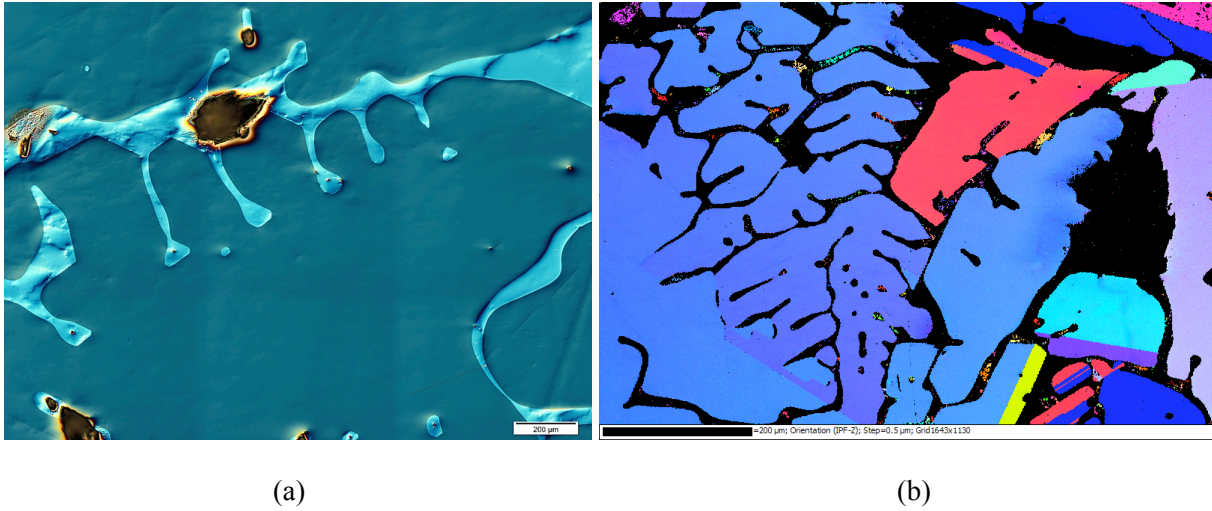


Figure 18. Optical image taken using a Nomarski prism of a small section of a growth from the  $\text{Cd}_{30}\text{Te}_{70}$  along with an EBSD map of small crucible growth at 1K/min cooling rate. Image in (a) shows  $\langle 110 \rangle$  growth instabilities near pinch-off with Te-particle faceting and solute trail formation. In (b) the EBSD map indicates large regions of single orientations and from this map the  $\langle 110 \rangle$  dendrite arms can be easily deduced.

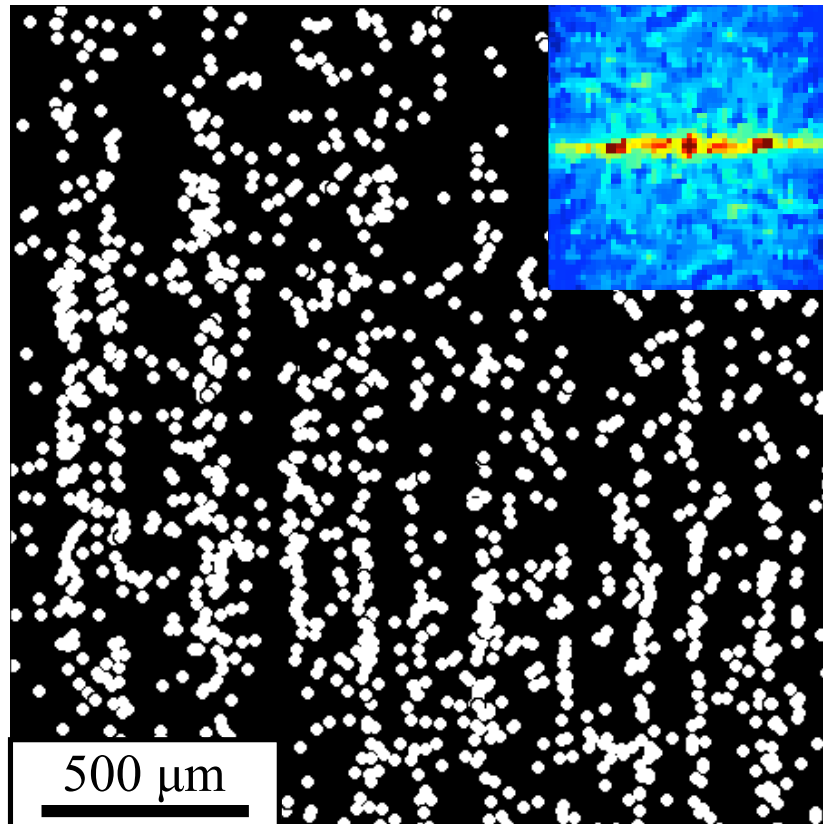


Figure 19. Positions of  $r_1$  size class Te-particles from TIR microscopy in a volume element from section 1 after rotating the volume parallel to  $\langle 110 \rangle$  and edge on to (111)-type planes. Ribbons or planar arrangements of Te-particles are clearly visible in the spatial arrangement. The inset figure shows the 2D Fourier transform (averaged) of the spatial arrangement of the data. The 1D arrangement of peaks in the Fourier transform indicate a horizontal spacing of approximately 145 microns.

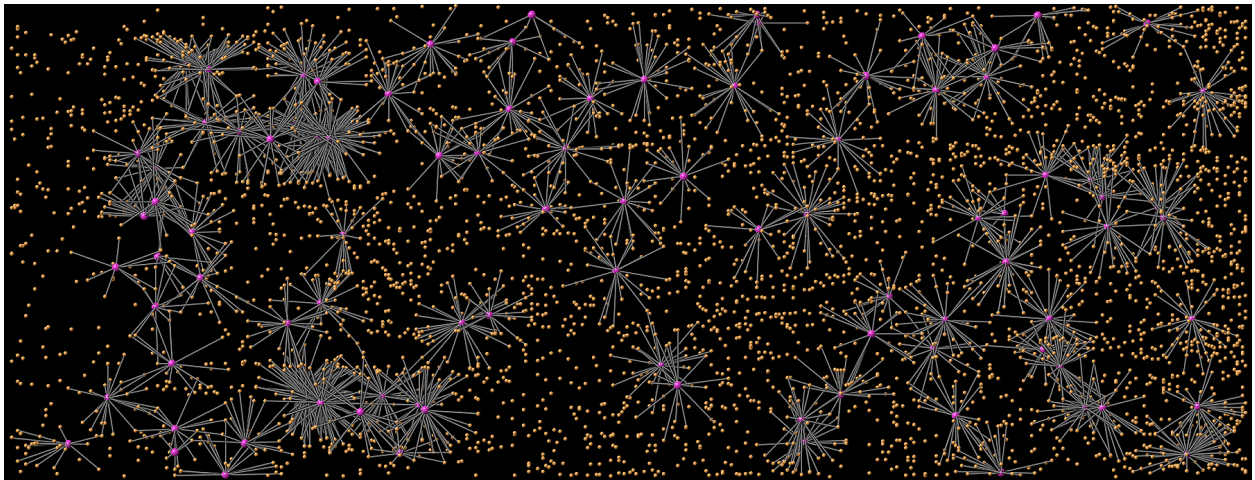
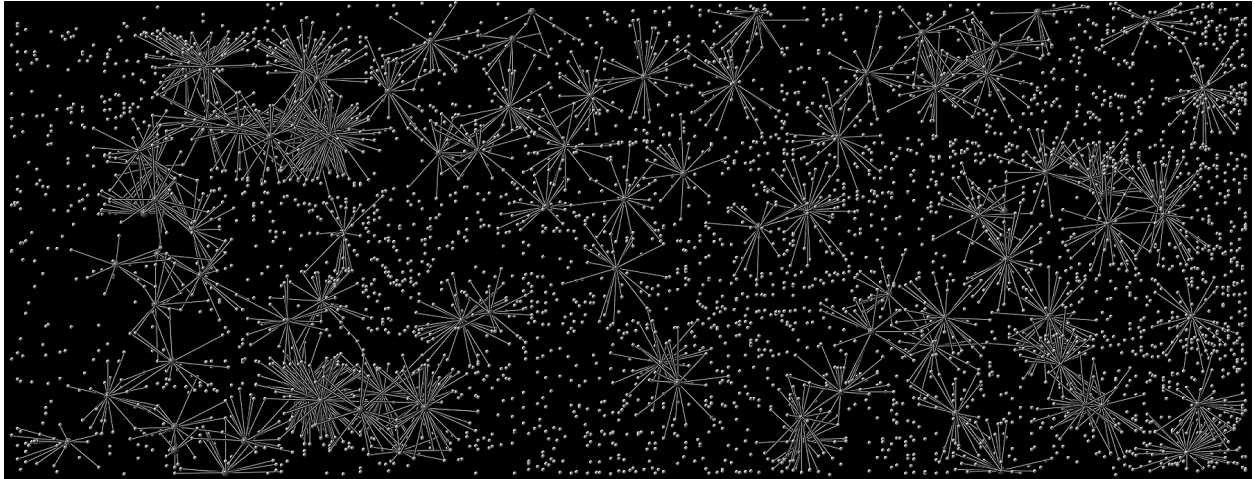


Figure 20. An image manipulated to show the large  $r_3$  Te-particles bonded to the nearest  $r_1$  Te-particles using stick bonds out to  $250\ \mu\text{m}$ . The closest  $r_1$  to  $r_3$  distance in this volume element is  $18\ \mu\text{m}$ .



**Pacific Northwest**  
NATIONAL LABORATORY

*Proudly Operated by **Battelle** Since 1965*

902 Battelle Boulevard  
P.O. Box 999  
Richland, WA 99352  
1-888-375-PNNL (7665)  
[www.pnnl.gov](http://www.pnnl.gov)



U.S. DEPARTMENT OF  
**ENERGY**